Lithos 252–253 (2016) 234–254

Contents lists available at ScienceDirect

Lithos

journal homepage: www.elsevier.com/locate/lithos

# Highly refractory peridotites in Songshugou, Qinling orogen: Insights into partial melting and melt/fluid–rock reactions in forearc mantle

Yi Cao [a,b,*], Shuguang Song [a,**], Li Su [c], Haemyeong Jung [b], Yaoling Niu [d,e]

[a] MOE Key Laboratory of Orogenic Belts and Crustal Evolution, School of Earth and Space Sciences, Peking University, Beijing 100871, China
[b] Tectonophysics Laboratory, School of Earth and Environmental Sciences, Seoul National University, Seoul 151-747, Republic of Korea
[c] Geological Lab Center, China University of Geosciences, Beijing 100083, China
[d] Department of Earth Sciences, Durham University, Durham DH1 3LE, UK
[e] Institute of Oceanology, Chinese Academy of Sciences, Qingdao 266071, China

ARTICLE INFO

*Article history:*
Received 25 September 2015
Accepted 3 March 2016
Available online 11 March 2016

*Keywords:*
Peridotite
Partial melting
Melt/fluid–rock reaction
Forearc mantle
Subduction zone
Qinling orogen

ABSTRACT

The Songshugou ultramafic massif is located in the eastern segment of the Qinling orogenic belt, central China. It is a large spinel peridotite body dominated by coarse-grained, porphyroclastic, and fine-grained dunite with minor harzburgite, olivine clinopyroxenite, and banded/podiform chromitite. The compositions of the bulk-rock dunite and harzburgite, and the constituent olivine and spinel, together with the textures and chemical characteristics of multiphase mineral inclusions, point to the highly refractory nature of these rocks with complex histories of high-temperature boninite melt generation and boninitic melt–rock reaction, probably in a young, warm, and volatile-rich forearc lithospheric mantle setting. Additionally, a subsequent low-temperature fluid–rock reaction is also recorded by $TiO_2$-rich spinel with Ti solubility/mobility enhanced by chloride- or fluoride-rich subduction-zone fluids as advocated by Rapp et al. (2010). The olivine clinopyroxenite, on the other hand, was likely crystallized from a residual boninitic melt that had reacted with harzburgitic residues. The ubiquitous occurrences of hydrous minerals, such as anthophyllite, tremolite, Cr-chlorite, and serpentine (stable at lower P–T crustal conditions) in the matrix, suggest that further low-temperature fluid–rock reaction (or retrograde metamorphism) has affected the original volatile-poor peridotites either in a mature and cool subduction zone, or in a continental crust during their exhumation into the Qinling collisional orogeny at early Paleozoic era, or both. The prolonged and intense ductile/brittle deformation can decrease the mineral grain size through dynamic recrystallization and fracturing, and thus aid the fluid–rock reaction or retrograde metamorphism and mineral chemical re-equilibration processes. Therefore, the Songshugou peridotites present a good example for understanding the petrogenesis and evolution of the mantle wedge, with the emphasis on the complex partial melting and melt/fluid–rock interactions in the forearc setting.



## 1. Introduction

The "tectonically emplaced" mantle rocks are generally referred to as peridotites that were tectonically exhumed from lithospheric mantle depths. They mainly occur as (1) dispersed ultramafic bodies in suture zones and orogenic belts (i.e. orogenic peridotite; multiple provenances), (2) basal sections of ophiolite or island arc complexes that are obducted onto land (sub-oceanic and sub-arc provenance), and (3) ultramafic rocks exhumed on the seafloor or above sea level by normal faults and/or serpentine diapirism (i.e. abyssal peridotite; sub-oceanic provenance) (see review of Bodinier and Godard (2007) and references therein). Among these tectonic environments, the forearc mantle above a subducting slab is the site of great complexity, where complicated interactions between partial melting, melt/fluid–rock reaction, and ductile deformation occur (e.g., Arai et al., 2007; Cao et al., 2015; Dai et al., 2011; Ionov, 2010; Ishii et al., 1992; Kaczmarek et al., 2015; Merle et al., 2012; Niu et al., 2003; Pal, 2011; Parkinson and Pearce, 1998; Pearce et al., 2000; Saka et al., 2014; Song et al., 2009; Soustelle et al., 2010; Uysal et al., 2015; Zhou et al., 2005). Therefore, understanding these diverse mantle processes and their interactions can expand our knowledge about the geodynamics of subduction zones, especially the forearc mantle processes. However, owing to the rare exposures of mantle peridotites in modern subduction zone, many above-mentioned mantle processes remain poorly understood in the setting of forearc region. As an alternative, the more common mantle peridotites derived from the ancient forearc mantle may be more informative regarding mantle processes over geological time. Such information is

* Correspondence to: Y. Cao, Tectonophysics Laboratory, School of Earth and Environmental Sciences, Seoul National University, Seoul 151-747, Republic of Korea.
** Corresponding author.
*E-mail addresses:* caoyi@snu.ac.kr (Y. Cao), sgsong@pku.edu.cn (S. Song).

http://dx.doi.org/10.1016/j.lithos.2016.03.002
0024-4937/

particularly important petrologically to understand mantle evolution from subduction initiation to subduction-zone magmatism, to closure of ocean basins, and to continental collision.

The Songshugou ultramafic massif offers us insights into these various processes. It was suggested to be tectonically emplaced into the Qinling orogenic belt, central China during the early Paleozoic era (e.g., Li et al., 2015; Tang et al., 2016). Over the past three decades, a large number of petrological and geochemical studies have been conducted on this ultramafic massif and its surrounding rocks (e.g., Dong et al., 2008; Lee et al., 2010; Liu et al., 1995, 2007; Song et al., 1998; Su et al., 2005; Tang et al., 2016; Wang et al., 2005; Yu et al., 2016; Zhang, 1995). However, its petrogenesis and tectonic setting still remain ambiguous. For example, some proposed that it is a tectonically emplaced Alpine-type (Li et al., 1991) or cumulate body (Song et al., 1998; Wang et al., 2005), or a segment of a mid-ocean ridge (MOR) ophiolitic mantle (either residue or cumulate or both) (e.g., Lee et al., 2010; Zhang, 1995). Others claimed that it represents a melt–rock reaction product associated with mantle plume activity without clarifying its tectonic setting (Liu et al., 2007; Su et al., 2005).

In this study, we present new mineral chemical data from the peridotites that show different textural and lithological characteristics. In particular, we characterized the texture and composition of multiphase inclusions in olivine and spinel. These multiphase inclusions are commonly suggested to represent the crystallization products of melt which is trapped during growth/crystallization of spinel and olivine (e.g., Renna and Tribuzio, 2011; Spandler et al., 2005). Owing to the protection by their competent host minerals, these inclusions are exempt from post-entrapment alterations and can thus be used as an effective tool for deciphering the parental magma compositions, so as to reveal some complex magmatic processes, such as magma mixing, assimilation and fractionation (e.g., Spandler et al., 2000, 2005). Combining these data with previously reported whole-rock geochemical data, we infer that the Songshugou ultramafic massif represents a highly refractory mantle remnant that was once situated in a young and warm (i.e. infant) forearc setting. These results provide us new insights into mantle melting, melt/fluid–rock interaction, and retrograde metamorphism, as well as their relationships with deformation in response to subduction and/or continental collision.

## 2. Geological setting

The Qinling orogen is a major NWW–SEE-trending orogenic belt in central China, separating the North China Craton to the north and the Yangtze Craton to the south (Fig. 1a). Connected eastwards with Dabie orogen, the Qinling–Dabie evolution comprises multiple and prolonged subduction–accretion–collision events in the Grenvillian (e.g., Chen et al., 1991), Neoproterozoic (e.g., Wang et al., 2003), Paleozoic (Cambrian: e.g., Yang et al. (2003), Carboniferous: e.g., Sun et al. (2002), and Triassic (e.g., Okay et al., 1993) (see recent review by Dong and Santosh (2016)). The Qinling orogen can be divided into the

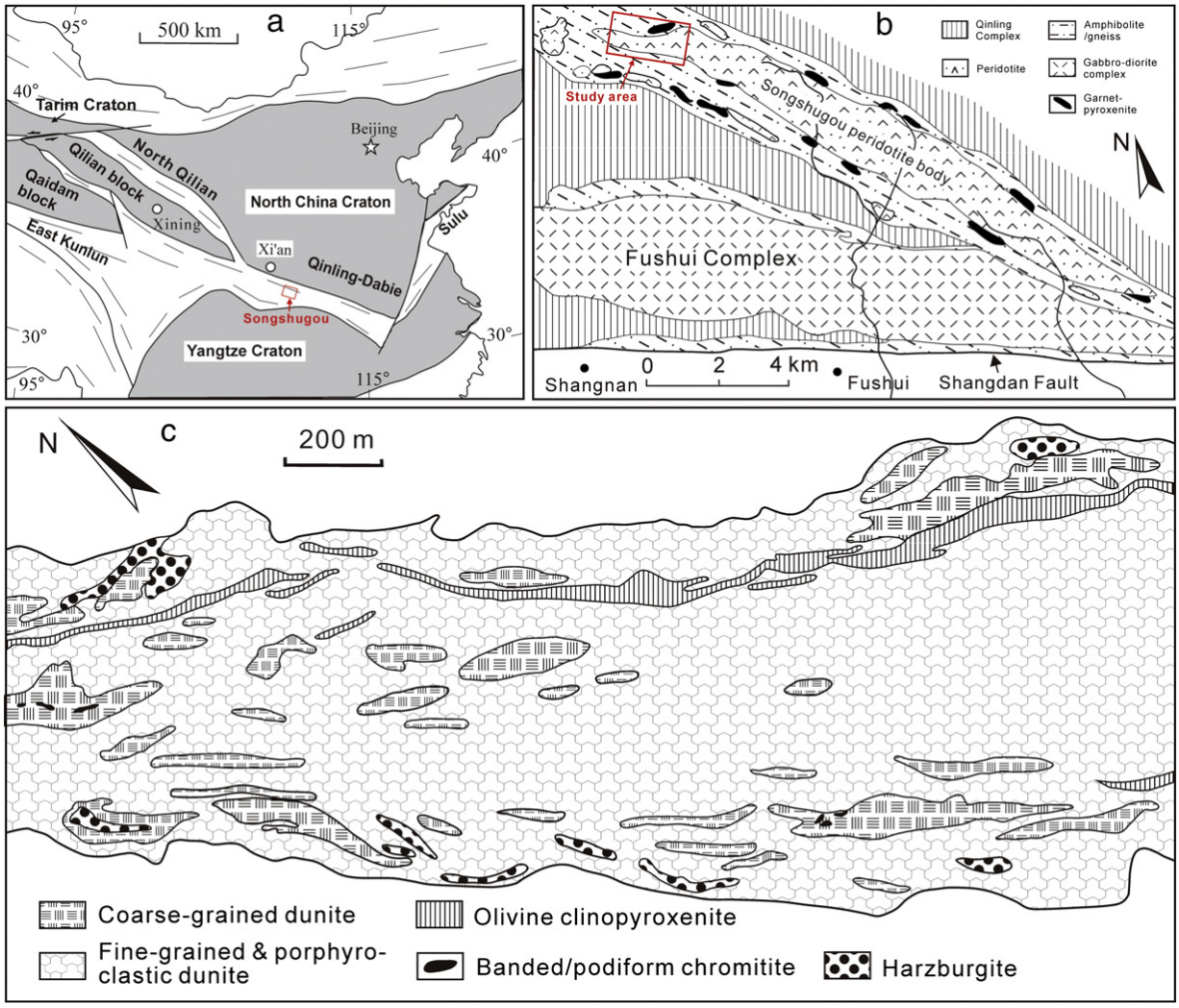


**Fig. 1.** (a) Geological map showing the major tectonic units in China. The location of Songshugou area is denoted by red box (b) Regional geological map of the Songshugou area showing the major structural and lithological unites. The study area is marked in red box. (c) Enlarged geological map showing the main types of ultramafic rock in the study area. (a) Modified after Song et al. (2013). (c) Modified after Su et al. (2005). (For interpretation of the references to color in this figure legend, the reader is referred to the web version of this article.)

north and south Qinling belts by the Shangdan Fault zone (e.g., Meng and Zhang, 2000; Ratschbacher et al., 2003). The Songshugou ultramafic massif is a large (~20 km$^2$; maximum width ~ 2 km and length ~ 20 km), fault-bounded, lentoid, NW–SE-trending spinel peridotite massif. It is situated in the core region of the Qinling Complex within the Shangdan suture zone, which is a Paleozoic subduction-zone complex consisting of garnet-amphibolite, garnet-pyroxenite, and high-pressure granulite (e.g., Liu et al., 1995; Tang et al., 2016; Fig. 1b). The boundaries between the ultramafic massif and its surrounding meta-mafic rocks are tectonic and are characterized by intense ductile deformation and mylonitization (Dong et al., 2008). The meta-mafic rocks are thought to have retrogressed from an eclogitic protolith by decompression during continental collision, based on the occurrence of symplectitic omphacite and estimated eclogite-facies P–T conditions (P ~ 2.2–2.5 GPa, T ~ 500 °C) (Bader et al., 2012; Liu et al., 1995). These rocks also record a high-pressure granulite-facies overprinting (P ~ 1.5–2.0 GPa, T ~ 750–880 °C) probably as a result of contact heating by the warm uplifting/uplifted ultramafic rocks (Bader et al., 2012; Li et al., 2009; Liu et al., 1995; Tang et al., 2016).

The formation age of the Songshugou ultramafic massif was poorly constrained hitherto, despite some metamorphic ages of surrounding rocks reported in the literatures. Recent U–Pb dating of zircons in high-pressure granulite and garnet pyroxenite yielded metamorphic ages of 480–515 Ma (Chen et al., 2004; Li et al., 2009; Liu et al., 2009; Su et al., 2004; Tang et al., 2016; Yu et al., 2016), which is most likely coeval with the ultramafic massif emplacement (because it resulted in contact heating and metamorphism of the surrounding mafic rocks, see above). These ages thus indicate that the exhumation of this ultramafic massif probably resulted from continental collision during the early Paleozoic era.

## 3. Petrography

The Songshugou ultramafic massif mainly consists of fresh dunite with minor harzburgite, olivine clinopyroxenite, and banded/podiform chromitite (Lee et al., 2010) (Fig. 1c). On the basis of field and petrographic characteristics, these ultramafic rocks can be roughly divided into four categories (e.g., Song et al., 1998; Su et al., 2005), discussed as follows. Mineral inclusions in these rocks are also described at the end of this section.

### 3.1. Fine-grained and porphyroclastic dunites

The fine-grained and porphyroclastic dunites are the dominant rock type and occupies up to 85% of the massif area. They consist of ~90 vol.% fine-grained (~150–250 μm) olivine with minor amphibole (mostly anthophyllite + minor tremolite), chlorite, serpentine, talc, and spinel. The specimens are strongly deformed with foliation clearly defined by well olivine layering and oriented acicular olivine-penetrating amphibole crystals (Fig. 2a). Occasionally, large olivine porphyroclasts or aggregates occur as relic lenses in the foliated and fine-grained matrix, which is composed of olivine, amphibole, serpentine, and talc (Fig. 2b). The spinel crystals are intensively fractured and elongated with a shape-preferred orientation subparallel to the foliation (Fig. 3a).

### 3.2. Coarse-grained dunite

This rock type crops out as lentoid blocks of various sizes and makes up ~10% of the massif area (Fig. 1c). In contrast to fine-grained and porphyroclastic dunite, most coarse-grained dunite has large (~600–1000 μm) and weakly oriented olivine grains (Fig. 2c and d). Some coarse-grained dunite samples also contain spinel-rich layers (thus locally disseminated chromitite) (Fig. 2d). Undulatory extinction and subgrain boundaries are observed in some olivine crystals (Fig. 2c). Euhedral amphibole (mostly anthophyllite + minor tremolite) crystals crosscut olivine grains randomly (Fig. 2c), and occasionally form orientated amphibole-rich layers. The amphibole mode is highly variable between samples, ranging from nearly amphibole-free to amphibole-rich (up to ~15 vol.%) compositions (i.e. amphibole dunite). The spinel grains are mostly euhedral to subhedral with uniform composition in the core and mantle (Fig. 3b). Anhedral spinel crystals are also observed (Fig. 3d).

### 3.3. Harzburgite

Similar to coarse-grained dunite, harzburgite occurs as lenses or boudins in the matrix of fine-grained dunite (Fig. 1c). Both coarse- and fine-grained harzburgites were reported in the literatures (Chen, 2004; Lee et al., 2010; Liu et al., 2007; Su et al., 2005; Wang et al., 2005). The mineral assemblage is composed of olivine, orthopyroxene (Opx), and amphibole (mostly anthophyllite) with minor spinel. The Opx grains show few exsolution lamellae (Fig. 2g and h), which is consistent with their low CaO content (see Section 4.3). The Opx mode is highly variable and it can reach up to ~80 vol.% in some samples. The shape of spinel crystals is similar to those in the coarse-grained dunite, while some spinel crystals show patchy compositional pattern (Fig. 3c). Only one coarse-grained sample was analyzed in this study. Amphibole grains (~40 vol.%, mostly anthophyllite) either crosscut olivine and Opx crystals randomly or form oriented amphibole-rich layers (Fig. 2e). In the weakly amphibolitized regions, the Opx grains have irregular boundaries surrounded by fine-grained olivine or fine-grained amphibole crystals (Fig. 2g), and some Opx crystals have olivine "inclusions" (olivine possibly penetrated along the fractures of Opx) (Fig. 2g). In some samples previously analyzed by Su et al. (2005), a poikilitic texture for Opx was also observed (Fig. 2h).

### 3.4. Olivine clinopyroxenite

Olivine clinopyroxenite occurs as 1–5 m-wide dykes within the northern part of the fine-grained dunite (Fig. 1c). It is weakly deformed and shows a mosaic texture. The mineral assemblage is characterized by clinopyroxene (Cpx), olivine, amphibole (mostly tremolite) with minor chlorite, serpentine and spinel. The Cpx grains occur as megacrysts (up to ~1 cm) in the fine-grained matrix, and commonly have Opx rhombs that are indicative of exsolution texture (Fig. 2f).

### 3.5. Mineral inclusions

Two types of mineral inclusions were recognized: (1) monophase mineral inclusions, and (2) multiphase (or polymineralic) inclusions. The monophase inclusions are frequently observed, such as oblate Opx inclusion in olivine (Fig. 4a) and acicular amphibole and chlorite inclusions in olivine and spinel (Fig. 4a, d and e). In contrast, the multiphase mineral inclusions are less common and mainly found in olivine and spinel in both coarse- and fine-grained dunite (especially spinel-rich coarse-grained dunite (SSG-2) and spinel-poor coarse-grained dunite (S03-2A)). The multiphase inclusions are mostly round, oval and elongated in shape (10–100 μm in max. Length) (Figs. 3d and 4b–f), and contain silicate minerals (e.g., olivine, Opx, Cpx, tremolite, and chlorite) with minor carbonate minerals (e.g., dolomite and magnesite) and oxides (e.g., spinel and magnetite). Despite difference in the identity of their included phases, similar morphology of multiphase inclusion (especially those round ones) was also documented in spinel and olivine grains from chromitite and peridotites within layered mafic-ultramafic intrusions (Li et al., 2005; Spandler et al., 2005; Veksler et al., 1998) and ophiolites (Arai et al., 1997; Renna and Tribuzio, 2011; Schiano et al., 1997).

## 4. Mineral chemistry

Mineral compositions were analyzed using a JEOL JXA-8100 electron probe micro-analyzer (EPMA) at Peking University. The measurement

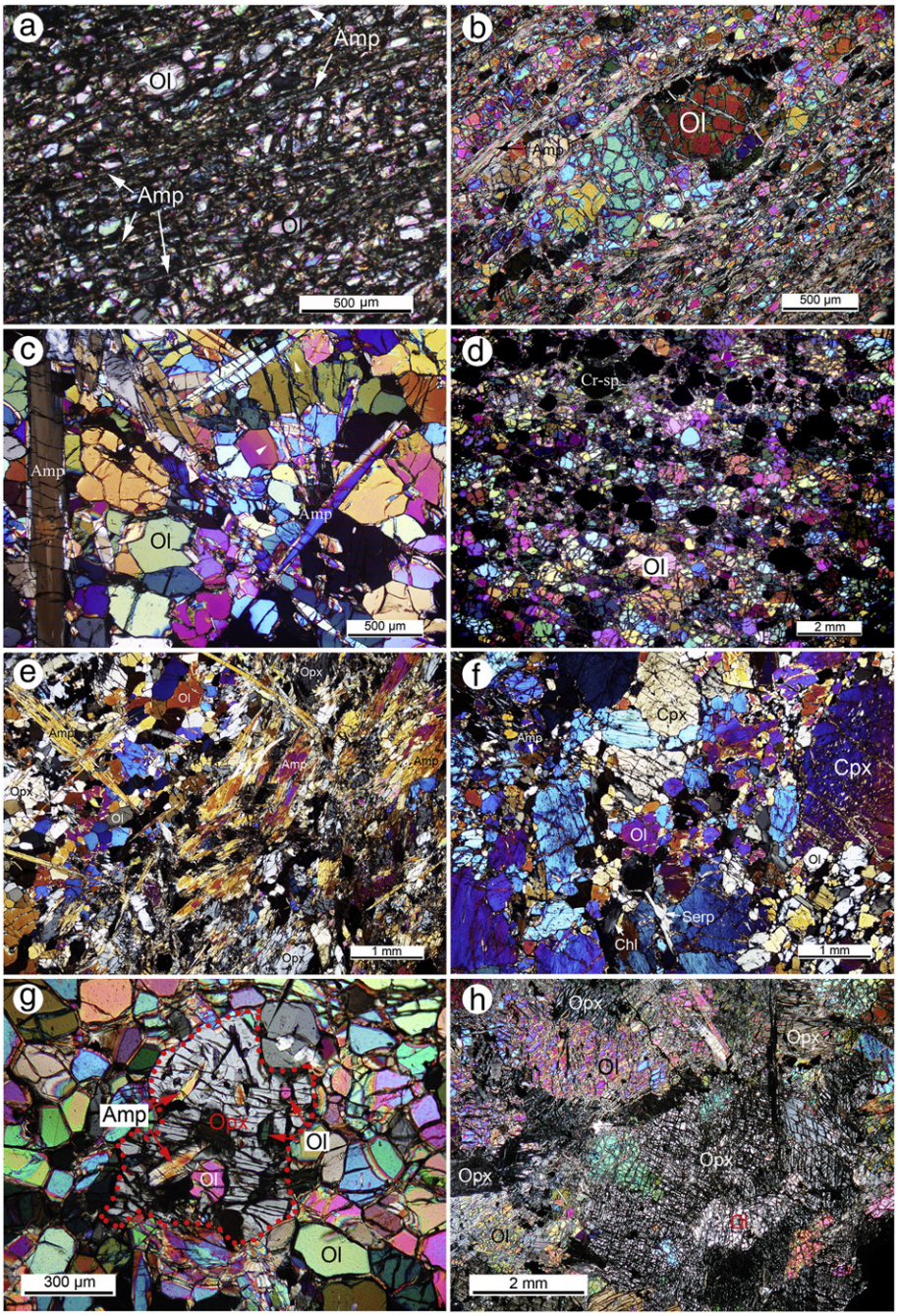


**Fig. 2.** Photomicrographs showing the textures of (a–d) dunite, (e, g, and h) harzburgite and (f) olivine clinopyroxenite. (a) Fine olivine grains and acicular amphibole (mostly anthophyllite) crystals forming a well-developed foliation in fine-grained dunite (S91-03). (b) Large lentoid olivine porphyroclasts occurring in the fine-grained and hydrated olivine matrix in porphyroclastic dunite (S-05). (c) Large columnar amphibole (anthophyllite) randomly crosscutting olivine grains in the spinel-poor coarse-grained dunite (08S-32). Subgrain boundaries in olivine are indicated by white arrow heads. (d) Spinel-rich coarse-grained dunite exhibiting elongated olivine grains (lower left domain) and spinel layers (SSG-2). (e) A coarse-grained harzburgite showing two distinct domains (S03-2B): upper left domain — amphibole crystals crosscutting the Ol + Opx assemblage randomly; lower right domain — amphibole crystals (anthophyllite) oriented and aggregated into an amphibole-rich layer. (f) Cpx megacrysts occurring in the fine-grained matrix, which is composed of olivine, amphibole (tremolite), serpentine, and chlorite in olivine clinopyroxenite (S91-32). (g) An irregularly shaped Opx crystal (outlined with the red dotted line) penetrated by small Amp (Anth) + Ol grains and embayed by fine-grained olivine grains in a harzburgite sample (S-27). (h) Poikilitic Opx texture in a coarse-grained harzburgite sample (S-249) (Su et al., 2005). (For interpretation of the references to color in this figure legend, the reader is referred to the web version of this article.)

was conducted using SEM conditions of 15 kV acceleration voltage, a 10 nA beam current, 1 μm beam spot and 20s counting time. The relevant standard minerals (from SPI corp. US) were used for calibration. The final results were corrected using the PRZ method (Goldstein et al., 2003). The chemical compositions of major constituent minerals and inclusions were measured in the core region of grains, to minimize the effect of mineral composition re-equilibrium during the cooling process. The formulae of minerals were calculated using the AX 2.0 program (details of AX program can be obtained from Tim Holland's web page https://www.esc.cam.ac.uk/research/research-groups/holland/ax). Additional compositional data of olivine and spinel from 5 harzburgite and 4 olivine clinopyroxenite samples were taken from Wang et al. (2005). The complete mineral compositional data are given in supplementary file (Table S1).

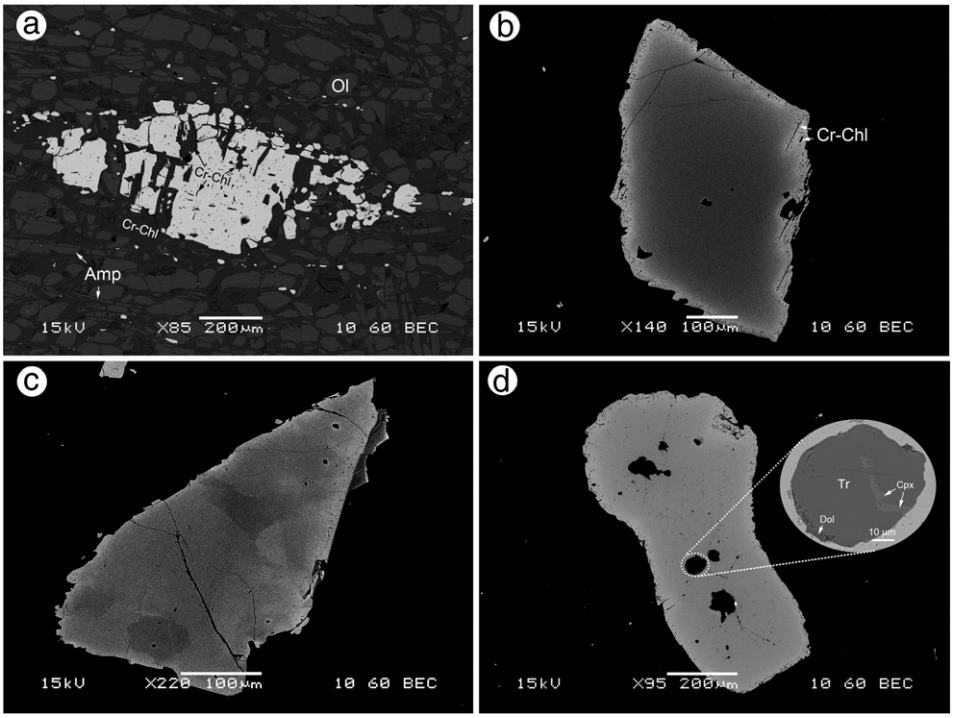


**Fig. 3.** Backscattered electron images showing the textures of spinel grains. (a) Extensively fractured and dismembered spinel grain in fine-grained dunite (S91-03). Intensive alteration by hydrous minerals (mostly chlorite) along the fractures, cleavage and rims of spinel. This spinel grain is fairly homogeneous in composition and oriented conformably with the overall foliation. (b) Euhedral rhomb-shaped spinel in spinel-poor coarse-grained dunite (08S-32). This spinel grain shows homogeneous compositions in the core and mantle, and a bright rim characterized by higher Fe and lower Cr, Al, and Mg contents owing to the chemical re-equilibrium or alteration at subsolidus conditions. Abundant cleavages filled with Cr-chlorite (Cr-Chl) are also observed in the rim. (c) A subhedral spinel grain showing a patchy pattern of composition variations in coarse-grained harzburgite (S03-2B). (d) An anhedral spinel grain characterized by large voids filled with multiphase inclusions and by irregularly corroded grain boundary in spinel-poor coarse-grained dunite (08S-32). Inset in (d) shows a rounded multiphase inclusion consisting of dominant tremolite (Tr) with minor Cpx and dolomite (Dol).

### 4.1. Olivine

Olivine shows a narrow compositional variation of $Fo^{\#}$ (~91–93) in spinel-poor coarse-grained, porphyroclastic, and fine-grained dunites, as well as harzburgite, with NiO content ranging from 0.2 to 0.4 wt.% (Fig. 5a and b). In contrast, olivine in spinel-layered (spinel-rich) coarse-grained dunite has a higher $Fo^{\#}$ of 93–95, probably as the result of subsolidus Fe–Mg exchange between olivine and spinel (Irvine, 1965). These olivines also have a wider variation of NiO content ranging from 0.15 to 0.5 wt.%. Olivine in the olivine clinopyroxenite shows distinctly lower $Fo^{\#}$ (84–90) and NiO contents (avg. ~0.22 wt.%) than olivine in other rock types (Table 1).

### 4.2. Spinel (chromite)

The spinel is Cr-rich and has a wide range of chemical compositions among different peridotite types (Table 2). In coarse-grained dunite and harzburgite, spinel has a fairly homogenous composition in the core and mantle of most grains, whereas the rims show conspicuously higher Fe and lower Cr, Al, and Mg contents (Fig. 3b and c, see also Lee et al., 2010). In contrast, spinel in fine-grained dunite is fairly homogeneous across the entire grains, and similar to the rim composition of spinel in coarse-grained dunite (Fig. 3a). The $Fe^{3+}$–Cr–Al and $Y(Fe^{3+})[=Fe^{3+}/(Fe^{3+}+Cr+Al)]$ versus $X(Fe^{2+})[=Fe^{2+}/(Fe^{2+}+Mg)]$ diagrams (Fig. 5c and d) show that the spinel composition in the studied peridotites overall follows the Fe–Ti trend that is characterized by an increasing $Fe^{2+}/(Fe^{2+}+Mg)$ ratio and $Fe^{3+}$ content toward magnetite, from coarse-grained dunite and harzburgite, through porphyroclastic dunite, to fine-grained dunite and olivine clinopyroxenite. According to the compositional classifications, spinel belongs to chromite in the coarse-grained dunite and harzburgite, but it changes to ferri-chromite in the fine-grained dunite and olivine clinopyroxenite. The spinel-layered coarse-grained dunite has much lower $X(Fe^{2+})$ values than the spinel-poor coarse-grained dunite. The average $Cr^{\#}[=100*Cr/(Cr+Al)]$ of spinel increases from ~81 in coarse-grained dunite, through ~86 in porphyroclastic dunite, to ~91 in fine-grained dunite. The average $Cr^{\#}$ of spinel in the harzburgite (~78) and olivine clinopyroxenite (~90) are similar to those in the coarse- and fine-grained dunite, respectively (Fig. 5a, e and f). The $TiO_2$ content in spinel is higher in fine-grained dunite and olivine clinopyroxenite (0.2–1.0 wt.%) than those in harzburgite and coarse-grained and porphyroclastic dunite (<0.2 wt.%) (Fig. 5e). Notably, spinel in porphyroclastic dunite has the largest variations of $Cr^{\#}$ and $Fe^{2+}$ contents, which cover the main compositional ranges of spinel in other peridotite types (Fig. 5f).

### 4.3. Pyroxenes

The Opx in harzburgite is highly refractory as indicated by low $Al_2O_3$ (0.19–0.26 wt.%) and CaO contents (0.05–0.07 wt.%), and high $Mg^{\#}$ (~92). The Cpx in olivine clinopyroxenite is diopside and shows high $Mg^{\#}$ (~94–99) and $Cr_2O_3$ content (0.34–0.40 wt.%), and low $Al_2O_3$ (0.8–1.0 wt.%), $TiO_2$ (<0.01 wt.%), and $Na_2O$ (0.1–0.3 wt.%) contents.

### 4.4. Amphibole

Both ortho-amphibole and clino-amphibole were recognized in the studied peridotites. The ortho-amphibole is Mg-anthophyllite ($Mg^{\#}$ ~ 90) which is the dominant amphibole phase in dunite and harzburgite. In contrast, the clino-amphibole belongs to tremolite (Ca-rich) which is the dominant amphibole phase in the Ca-rich olivine clinopyroxenite. The tremolite is also characterized by relatively low $Na_2O$ (0.05–0.56 wt.%) and $Al_2O_3$ (0.5–1.4 wt.%) contents. The alteration

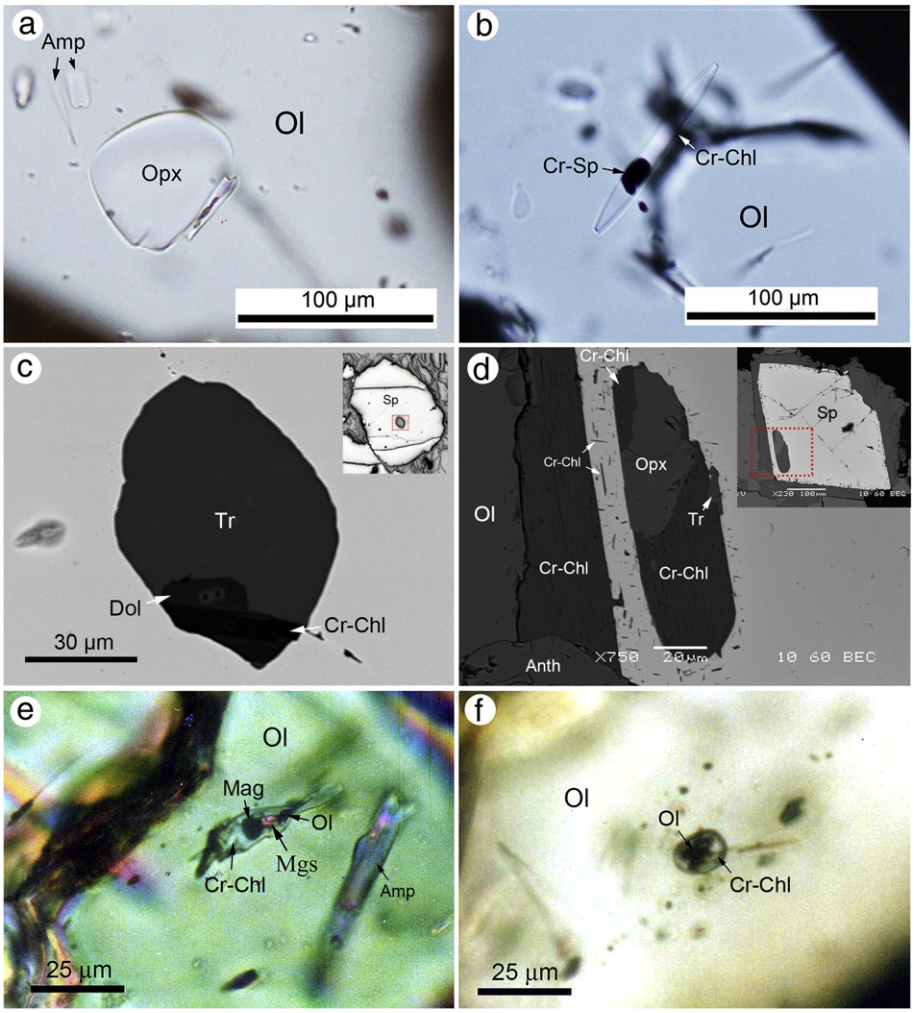


**Fig. 4.** Optical photomicrographs and backscattered electron images showing representative mono- and multi-phase inclusions in olivine and spinel. (a) Monophase inclusions: an oblate Opx crystal and small acicular amphibole needles in olivine in spinel-poor coarse-grained dunite (S03-2A). (b) A spindle-like Cr-spinel-bearing Cr-chlorite multiphase inclusion in olivine in spinel-poor coarse-grained dunite (S03-2A). (c) An oval multiphase mineral inclusion consisting of tremolite, dolomite, and Cr-chlorite in the core of spinel in spinel-rich coarse-grained dunite (see upper-right inset) (SSG-2). (d) A prolate multiphase inclusion consisting of Cr-chlorite, Opx, and minor tremolite in the rim of a rhombic spinel grain in spinel-poor coarse-grained dunite (see upper-right inset) (08S-32). Notably, the spinel grain is altered by Cr-chlorite as indicated by abundant minute acicular inclusions in the rim and platy corona in the neighboring matrix. (e) A fish-like multiphase inclusion in olivine in porphyroclastic dunite (S-05). It contains mainly Cr-chlorite and small crystals of magnesite, magnetite, and olivine. Nearby, a columnar olivine-penetrating amphibole crystal is observed. (f) Numerous ovoid multiphase inclusions containing olivine and Cr-chlorite in olivine in spinel-poor coarse-grained dunite (S-11). Mineral abbreviations: amphibole (Amp), anthophyllite (Anth), Cr-chlorite (Cr-Chl), dolomite (Dol), magnesite (Mgs), magnetite (Mag), olivine (Ol), orthopyroxene (Opx), spinel (Sp), and tremolite (Tr). Figure (e) and (f) were modified after Su et al. (2005).

texture in which large columnar tremolite crystals peripherally altered to fibrous anthophyllite is also occasionally observed.

### 4.5. Chlorite

The chlorite has a close association with spinel. It mostly occurs in the immediate vicinity of spinel (Fig. 4d), and resides along fractures in spinel (Fig. 3a and b). They display high $Cr_2O_3$ (1.6–3.3 wt.%) and relatively low $Al_2O_3$ (12.0–16.8 wt.%) contents, which classifies them as chromium chlorite ($Cr^{\#}$ ~ 6–12). Besides, the chlorite commonly has high MgO (32.1–34.6 wt.%) and low FeO (2.0–4.3 wt.%) contents, resulting in a very high $Mg^{\#}$ of 93–97.

### 4.6. Mineral inclusions

The compositional analyses show that amphibole in multiphase inclusion mostly belongs to tremolite, similar to the tremolite in the matrix (Table 3). Chlorite forms two types of inclusions and also shows similar compositions to those in the matrix (Table 3). The $Mg^{\#}$ of olivine and Opx inclusions is similar to those in the matrix. The carbonate inclusions are either magnesite or dolomite. In comparison to chlorite and olivine, other included phases appear to have a slightly higher $Cr_2O_3$ content than their counterparts in the matrix.

### 4.7. Sub-solidus equilibrium temperature

The sub-solidus equilibrium temperatures of the Songshugou peridotites were estimated using the olivine–spinel Mg–$Fe^{2+}$ exchange thermometer (Ballhaus et al., 1991). This temperature was calculated at an arbitrary pressure of 1.5 GPa which conforms with the stability of spinel-facies peridotite. The estimated temperatures show a descending order: spinel-rich coarse-grained dunite (955 ± 107 °C), spinel-poor coarse-grained dunite (826 ± 13 °C), coarse-grained harzburgite (809 ± 17 °C), porphyroclastic dunite (799 ± 29 °C), fine-grained dunite (757 ± 52 °C), and olivine clinopyroxenite (661 ± 34 °C).

## 5. Whole-rock major and trace element compositions

The major and trace element compositions of the Songshugou peridotites (excluding spinel-rich coarse-grained dunite) were taken from

previous studies (Chen, 2004; Lee et al., 2010; Liu et al., 2007; Su et al., 2005). The compositions were measured using X-ray fluorescence (XRF) and inductively coupled plasma mass spectrometry (ICP-MS). In this study, these original data were recalculated on a volatile-free basis, to correct for the dilution effect caused by later hydration or retrograde metamorphism processes (Parkinson and Pearce, 1998; Parkinson et al., 1992). The complete data of whole-rock compositions are given in the supplementary file (Table S2).

### 5.1. Major elements

In order to characterize the original mineral modal proportions in anhydrous ultramafic rocks, we calculated the olivine, orthopyroxene, clinopyroxene and spinel modes in their CIPW norm in low-pressure spinel-facies peridotite using whole-rock major element compositions (Niu, 1997). This CIPW norm calculation converts the modes of later-formed hydrous silicates such as amphibole and chlorite to those of their original anhydrous precursors such as pyroxene, olivine and spinel, and thus enables the comparisons of original mineral assemblages between anhydrous and various-degreed hydrated rocks. Because, for instance, Ca and Al (and Cr) are mainly transferred from clinopyroxene to tremolite and from spinel to chlorite, respectively (see Section 6.5.3), the estimated normative Cpx and Sp modes depend exclusively on the whole-rock concentrations of CaO and $Al_2O_3$. In other words, although the principle of CIPW norm calculation is conventionally based on the mineralogy precipitated from an anhydrous melt, it is still reliable to apply it for reconstructing the anhydrous mineral assemblage from those hydrated rocks such as this work.

It is important to note that many dunite samples actually fall in the harzburgite field (Fig. 6a). Therefore, it implies that a significant amount of Opx must have been consumed by low-T fluid–rock reactions or retrograde metamorphic reactions (see Sections 6.5.2 and 6.5.3) and that many "so-called" dunite samples are originally harzburgite. The mode of clinopyroxene is very low (<2.3%) in most recalculated dunite and harzburgite, except for one sample that plots in the olivine websterite field. Excluding two harzburgite samples that plot far away from the rest of the dunites and harzburgites, the harzburgite and dunite samples show a discernible trend of decreasing olivine mode with whole-rock magnesium number (Fig. 6b). All the olivine clinopyroxenite samples are located close to or within the field of olivine clinopyroxenite (Fig. 6a).

As shown in Fig. 6e and f, the $Al_2O_3$ and CaO contents are very low (<0.7 wt.%) in most harzburgite and dunite. Negative MgO–$SiO_2$, MgO–$Al_2O_3$, MgO–CaO, and positive MgO–FeOt trends are obvious when the two off-trend harzburgite samples are neglected (Fig. 6c–f). The MgO–$SiO_2$ and MgO–FeOt trends deviate remarkably from the melting curves, and they bridge the end of the melting curves and the region of olivine composition in the peridotites (see also Niu, 1997; Song et al., 2004).

### 5.2. Trace element characteristics

The chondrite-normalized REE patterns of the Songshugou peridotites are presented in Fig. 7a–e. Two subsets of coarse-grained dunite can be distinguished in terms of their REE patterns. Subset 1 shows very low REE abundances (REE concentration less than 0.1 chondrite), gentle U-shaped REE patterns, and a positive Eu anomaly, whereas subset 2 displays significantly higher REE concentrations (>0.1 chondrite), prominently elevated LREE, and flat MREE–HREE patterns with a weak-to-moderate negative Eu anomaly (Fig. 7a). Fine-grained dunite is overall similar to the subset 1 coarse-grained dunite in terms of their REE patterns, with or without the Eu anomaly (Fig. 7b). The REE patterns of coarse-grained harzburgite mimic those of the subset 2 coarse-grained dunite, without a discernible Eu anomaly (Fig. 7c). In contrast, the REEs define a pronounced U shape pattern without Eu anomaly in fine-grained harzburgite (Fig. 7d).

For comparison, we plot chondrite-normalized trace-element diagrams using the element incompatibility order from Parkinson et al. (1992) (Fig. 7f–j). As a whole, all peridotite samples exhibit spiked patterns on the left side of the diagram, in which Cs, Ba, U, and Ta are enriched relative to Rb, Th, and Nb. However, the most conspicuous exception to this generalization is that Th is not depleted but enriched in most coarse-grained dunite and harzburgite. Pronounced positive Sr anomalies and weak-to-moderate enrichments of Zr and Hf are also observed in most harzburgite and dunite. A strong Nb–Ta fractionation is also present in dunite and harzburgite (i.e. chondrite-normalized ratio Nb/Ta ≪ 1). These geochemical characteristics bear some similarities to the refractory harzburgite from the East Pacific Rise (EPR), as reported by Niu and Hekinian (1997). In addition, Y displays enrichment in fine-grained dunite and harzburgite, but shows no anomaly in coarse-grained dunite and harzburgite.

## 6. Discussion

### 6.1. Highly refractory residue after high-degree partial melting

Several lines of evidence suggest that the Songshugou harzburgite and dunite most likely represent a refractory mantle residue after a large extent of melt extraction. First, the nature of the melting residue can be inferred from the anhedral shape of spinel, which indicates melting or dissolution of spinel crystals, whereas euhedral spinel is more likely crystallized from a percolating melt (e.g., Dare et al., 2009). In the studied harzburgite and dunite samples, anhedral spinel can be observed (Fig. 3d). Second, because (1) the olivine shows a narrow $Fo^{\#}$ range (~91–93) in all spinel-poor harzburgite and dunite, and (2) an expected lower $Fo^{\#}$ (<90) olivine suite is absent from the harzburgites or lherzolites (Fig. 5a and b; see also Wang et al., 2005) and the latter were not found in the field, it is not reasonable to interpret these rocks as the products from fractional crystallization. Third, the inverse relationship between the olivine modes and whole-rock $Mg^{\#}$ (approximate to $Fo^{\#}$) may favor neither a simple fractional crystallization nor a solely cumulate origin for the harzburgite and dunite (Fig. 6b).

The main evidence for their high-degree melting, residual nature includes the following:

First, very low whole-rock CaO, $Al_2O_3$, and $TiO_2$ contents are observed in harzburgite and dunite. The whole-rock CaO, $Al_2O_3$, and $TiO_2$ can be progressively depleted with an increasing extent of melting, which enables their concentrations to be a good indicator of the extent of melting (Ishiwatari, 1985; Pearce et al., 1992). In most Songshugou harzburgites and dunites, the very low concentrations of whole-rock

**Fig. 5.** The compositions of olivine and spinel in the studied peridotites. (a) Olivine $Fo^{\#}$ vs spinel $Cr^{\#}$. Dashed arrow indicates the trend of increasing $Cr^{\#}$ and decreasing $Fo^{\#}$. OSMA is the olivine–spinel mantle array as proposed by Arai (1994). (b) Olivine NiO vs. olivine $Fo^{\#}$. The compositional fields of olivine in abyssal and forearc peridotite are from Dick (1989) and Ishii et al. (1992), respectively. Compositions of mantle olivine are also shown (Mantle Olivine Array) (Takahashi et al., 1987). The olivine compositions of $Fo^{\#}$ in the range of 84–87 and unknown NiO contents in olivine clinopyroxenite were taken from Wang et al. (2005) (vertical dashed line and black arrow). (c) Spinel $Fe^{3+}$–Cr–Al ternary diagram. The light and dark shading regions represent 90% and 50% of the entire terrestrial spinel data points, respectively. The light dash-dotted line and heavy dashed line enclose 90% and 50% of the entire spinel data points from boninite, respectively (Barnes and Roger, 2001). (d) Spinel $Fe^{3+}/(Fe^{3+}+Cr+Al)$ vs. spinel $Fe^{2+}/(Fe^{2+}+Mg)$. (e) Spinel $TiO_2$ content vs. spinel $Cr^{\#}$. Dashed lines denote the spinel compositions in Mg-rich magmas which were originated from different tectonic settings (Arai, 1992). The spinel compositions after variable degrees of partial melting of a fertile MORB (FMM) source (in fractional melting mode, 5–30%) are shown in the labeled curve (Pearce et al., 2000). Large gray arrows indicate sequentially (#1) high-temperature boninitic melt–rock reaction, (#2) low-temperature $TiO_2$-rich fluid–rock reaction, and (#3) chlorite-forming retrograde reaction that increases the $Cr^{\#}$ of remnant spinel. (f) Spinel $Cr^{\#}$ vs. spinel $Fe^{2+}/(Fe^{2+}+Mg)$. The compositional fields of spinel in mid-ocean ridge (MOR) peridotite, supra-subduction zone (SSZ) peridotite and boninite were from Dick and Bullen (1984), Ishii et al. (1992), and van der Laan et al. (1992), respectively. Sample symbols are shown in (a) and (b).

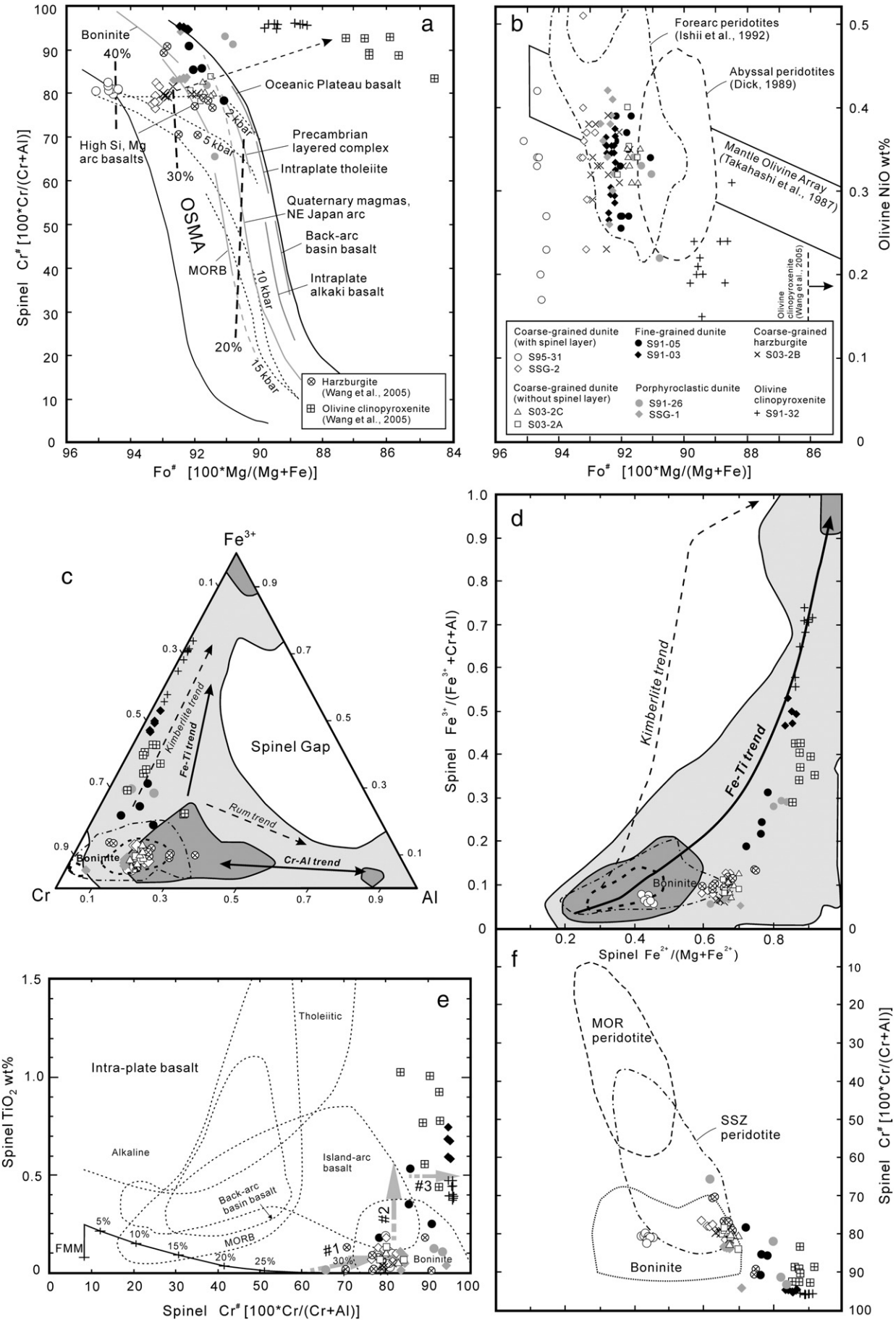
a
Boninite
40%
30%
20%
High Si, Mg arc basalts
OSMA
MORB
Oceanic Plateau basalt
2 kbar
5 kbar
10 kbar
15 kbar
Precambrian layered complex
Intraplate tholeiite
Quaternary magmas, NE Japan arc
Back-arc basin basalt
Intraplate alkaki basalt
Harzburgite (Wang et al., 2005)
Olivine clinopyroxenite (Wang et al., 2005)
Spinel Cr# [100*Cr/(Cr+Al)]
Fo# [100*Mg/(Mg+Fe)]
b
Forearc peridotites (Ishii et al., 1992)
Abyssal peridotites (Dick, 1989)
Mantle Olivine Array (Takahashi et al., 1987)
Olivine clinopyroxenite (Wang et al., 2005)
Coarse-grained dunite (with spinel layer)
S95-31
SSG-2
Fine-grained dunite
S91-05
S91-03
Coarse-grained harzburgite
S03-2B
Coarse-grained dunite (without spinel layer)
S03-2C
S03-2A
Porphyroclastic dunite
S91-26
SSG-1
Olivine clinopyroxenite
S91-32
Olivine NiO wt%
Fo# [100*Mg/(Mg+Fe)]
c
Fe3+
Cr
Al
Spinel Gap
Kimberlite trend
Fe-Ti trend
Rum trend
Cr-Al trend
Boninite
d
Kimberlite trend
Fe-Ti trend
Boninite
Spinel Fe3+ /(Fe3+ +Cr+Al)
Spinel Fe2+ /(Mg+Fe2+)
e
Tholeiitic
Intra-plate basalt
Alkaline
Island-arc basalt
Back-arc basin basalt
MORB
FMM
5%
10%
15%
20%
25%
30%
#1
#2
#3
Boninite
Spinel TiO2 wt%
Spinel Cr# [100*Cr/(Cr+Al)]
f
MOR peridotite
SSZ peridotite
Boninite
Spinel Cr# [100*Cr/(Cr+Al)]

$Al_2O_3$ (<0.7 wt.%) and CaO (<0.7 wt.%), thus indicate 30–33% melting (in batch melting mode), and the low $TiO_2$ (<0.01 wt.%) corresponds to over 20% melting (in fractional melting mode). Because the concentrations of $TiO_2$ are below the detection limit of XRF analysis and more precise data measured by ICP-MS are not available, the whole-rock $TiO_2$ content used in this study can only be considered as an upper limit and 20% fractional melting should thus be considered as a lower-bound estimate.

Second, the whole-rock composition data from dunite and harzburgite samples link the melting curves at the high-degree end (~25% partial melting in both batch and fractional melting modes) with compositions of olivine in MgO–$SiO_2$ and MgO–FeOt diagrams (Fig. 6c and d). This characteristic implies that these harzburgite and dunite had been melted about 25%, and then enriched with excess olivine that can be produced through olivine crystallization/precipitation either from olivine-saturated percolating melt during ascent or by replacing pyroxene (mostly Opx) during the melt–peridotite reaction (e.g., Kelemen et al., 1995; Niu, 1997; Niu et al., 1997).

Third, depleted whole-rock HREE patterns are presented in harzburgite and dunite (Fig. 7a–d). The extent of partial melting in mantle peridotite can also be inferred from the abundance of whole-rock HREEs, because the abundance of these elements is inversely correlated with the degree of partial melting but is only slightly affected by later retrograde metamorphism or metasomatic processes (Hellebrand et al., 2001). Compared with the calculated chondrite-normalized whole-rock REE patterns of residual peridotite after variable melting degrees (Piccardo et al., 2007), except for subset 2 coarse-grained dunite, the measured REE abundances (<0.1 chondrite) and patterns of the harzburgite and dunite can best be matched by the REE patterns after 23–27% melting (in fractional melting mode). The exact reasons for the distinct REE patterns of the subset 2 coarse-grained dunite are not clear. However, their elevated LREE–HREE concentrations might imply that significant quantities of both LREE and HREE could be retained if large porosities can somehow be present in the rock during melting. Because the Cpx is the main host of REEs (especially HREEs) in the anhydrous peridotite, the similar calculated Cpx mode (converted from tremolite, see Section 6.5.3) or whole-rock CaO content between subset 1 and 2 coarse-grained dunite (Table S2) indicate that their distinctive REE contents are not correlated with original Cpx modes, but likely related to different REE concentrations in original Cpx.

The modal proportion of Cpx is a good measure of the degree of melting of lherzolite to harzburgite (e.g., Dick and Fisher, 1984; Niu, 1997), because Cpx is a moderately abundant phase that is consumed rapidly during anhydrous melting of a spinel lherzolite (Jaques and Green, 1980):

$$\mathrm{Cpx} + \mathrm{Opx} + \mathrm{olivine}_1 + \mathrm{spinel}_1 = \mathrm{olivine}_2 + \mathrm{spinel}_2 + \mathrm{melt}_1 \quad (1)$$

modified after Niu (1997). $Olivine_1$, $spinel_1$ and $olivine_2$, $spinel_2$ indicate the original and newly-formed olivine and spinel during partial melting, respectively, whereas $melt_1$ is the produced melt with composition depending on the degree of melting. Therefore, a peridotite that contains 15 vol.% compared to one that contains 0 vol.% Cpx correspond approximately to initiation of melting and to above ~25% of melting (in batch melting mode), respectively (Dick and Fisher, 1984; Niu, 1997). In fact, a minor amount of Cpx may still persist to above ~25% melting if melting occurs in a hydrous condition (Gaetani and Grove, 1998). Owing to the reactions with silica-undersaturated melts (consuming pyroxenes, see section below), the mode of clinopyroxene in our harzburgite and dunite can actually not be used to infer the degree of melting. However, most harzburgite or dunite samples show a very low recalculated modal abundance of Cpx (<2.3%) in the recalculated Ol–Opx–Cpx mineral assemblage (Fig. 6a). Assuming that Cpx is solely consumed during partial melting, this small Cpx mode thus indicates at least 25% batch melting, which is consistent with the melting degree inferred from other methods above. This result, on the other hand, also implies that most Cpx was consumed during partial melting, and that subsequent melt/fluid–rock interactions (see section below) thus only slightly modified the Cpx mode.

Collectively, we conclude that the Songshugou harzburgite and dunite are highly refractory mantle residues that have experienced 25–33% (in batch melting mode) or 23–27% (in fractional melting mode) melting. Because fractional melting is more efficient in extracting the incompatible components than batch melting, a relatively larger degree of batch melting is required to produce the same extent of depletion as fractional melting.

### 6.2. High-temperature melt–rock reactions

Commonly, the refractory mantle composition after intensive melting can be modified subsequently by interaction with percolating melt/fluid. The melt/fluid–rock reaction process can also be proved in the Songshugou harzburgite and dunite.

The first evidence comes from the mineral dissolution textures. The irregular grain boundaries of Opx in contact with fine-grained olivine crystals (Fig. 2g), the poikilitic Opx texture (Fig. 2h), and the oblate Opx inclusion in olivine grains (Fig. 4a) indicate that the Opx was either dissolved by a percolating reactive melt or incongruently melted to form olivine during partial melting (e.g., Bédard et al., 2009; Dai et al., 2011; Edwards and Malpas, 1995; Zhou et al., 2005). The euhedral spinel grains may imply that they were directly crystallized from the reacting melt (Fig. 3b). Some subhederal spinel crystals showing a patchy composition pattern may suggest the mixing and overgrowing of old spinel grains during melt–rock reaction (Fig. 3c).

Second, significant enrichments of some LREEs and HFSEs (e.g., Ta, Zr, and Hf) are presented in harzburgite and dunite. The high LREE/MREE ratios (U-shaped REE patterns), and elevated Ta, Zr, and Hf concentrations in most harzburgite and dunite samples (Fig. 7a–d and f–i)—because their partition coefficients between olivine and silicate melt are relatively greater compared to other trace elements, see Bédard (2005)—clearly suggest that these rocks were not simply formed by melting the fertile mantle, but also pervasively refertilized due to subsequent melt/fluid–rock reactions (e.g., Dai et al., 2011; Parkinson et al., 1992; Song et al., 2004). However, the very strong Nb–Ta fractionation ($Nb/Ta \ll 1$) may be in line with their extremely depleted origin (Niu and Hekinian, 1997). In a similar manner, the pronounced spikes of fluid-mobile large ion lithophile elements (LILEs; Cs, Ba, U, and Sr) could be interpreted as enrichments due to interaction between an aqueous agent (e.g., aqueous fluid or hydrous melt) and the depleted mantle residue.

Third, it is generally accepted that a high $Fo^{\#}$ in olivine ($olivine_2$) and a high $Cr^{\#}$ in spinel ($spinel_2$) are indicators of the highly refractory mantle (e.g., Arai, 1994; Dick and Fisher, 1984; Matsukage and Kubo, 2003). However, the very high $Cr^{\#}$ of spinel (>70) in dunite is most likely produced by a melt–rock reaction, rather than high-degree melting (Zhou et al., 1996, 2005). As shown in Fig. 5a, almost all the harzburgite and dunite samples fall within the high $Fo^{\#}$ and $Cr^{\#}$ region of the olivine–spinel mantle array (OSMA) of Arai (1994). The few spinel-layered dunites show (1) apparently higher $Fo^{\#}$ in olivine (Fig. 5a and b) which may result from a more extensive Fe–Mg exchange between olivine and spinel under subsolidus conditions (Irvine, 1965); and (2) higher $Mg^{\#}$ in spinel (Fig. 5d) which may represent the original composition, because the high model abundances of spinel can prevent significant modification of spinel composition during chemical re-equilibration with olivine (Barnes and Roger, 2001). The olivine $Fo^{\#}$ (~91–93) in spinel-poor dunite and harzburgite is exempted from significant low-T Fe–Mg partitioning effect with the minor spinel and clinopyroxene, whereas the $Mg^{\#}$ in spinel is strongly modified (see section above) (Evans and Frost, 1975; Obata et al., 1974). Therefore, the compositions of olivine ($Fo^{\#}$ ~ 91–93) and spinel ($Cr^{\#}$ ~ 76–84) in spinel-poor coarse-grained dunite and harzburgite are indicative of a residual origin after 25–33% melting (in batch melting mode) at ~0.2 GPa (Jaques and

**Table 1**
Representative composition of olivine.

| Rock type | Coarse-grained dunite | | | | | | | | Porphyroclastic dunite | | | | Fine-grained dunite | | | | Harzburgite | | Olivine clinopyroxenite | |
|---|---|---|---|---|---|---|---|---|---|---|---|---|---|---|---|---|---|---|---|---|
| Sample | SSG-2[a] | | S95-31[a] | | S03-2A[b] | | S03-2C[b] | | S91-26 | | SSG-1 | | S91-03 | | S91-05 | | S03-2B | | S91-32 | |
| $SiO_2$ | 40.37 | 40.93 | 41.34 | 41.70 | 41.18 | 41.34 | 40.91 | 41.14 | 40.85 | 40.53 | 41.51 | 41.34 | 40.44 | 40.56 | 40.32 | 40.48 | 40.84 | 41.09 | 40.46 | 40.60 |
| $TiO_2$ | 0.00 | 0.01 | 0.01 | 0.00 | 0.00 | 0.03 | 0.00 | 0.07 | 0.00 | 0.00 | 0.02 | 0.00 | 0.00 | 0.00 | 0.01 | 0.00 | 0.00 | 0.00 | 0.00 | 0.00 |
| $Al_2O_3$ | 0.00 | 0.01 | 0.04 | 0.03 | 0.00 | 0.00 | 0.00 | 0.00 | 0.00 | 0.00 | 0.00 | 0.01 | 0.00 | 0.00 | 0.00 | 0.01 | 0.00 | 0.00 | 0.00 | 0.00 |
| $Cr_2O_3$ | 0.00 | 0.02 | 0.00 | 0.02 | 0.00 | 0.05 | 0.03 | 0.33 | 0.00 | 0.02 | 0.04 | 0.00 | 0.01 | 0.01 | 0.00 | 0.01 | 0.02 | 0.00 | 0.10 | 0.00 |
| $Fe_2O_3$ | 0.83 | 0.83 | 0.43 | 0.22 | 0.00 | 0.38 | 0.00 | 0.05 | 0.00 | 0.58 | 0.00 | 0.00 | 0.91 | 0.93 | 1.00 | 0.97 | 0.41 | 0.85 | 0.21 | 0.60 |
| FeO | 6.72 | 6.70 | 5.30 | 4.90 | 8.28 | 7.80 | 8.32 | 8.01 | 8.88 | 8.15 | 7.52 | 7.50 | 7.35 | 7.51 | 8.10 | 7.86 | 7.59 | 6.89 | 10.92 | 10.23 |
| MnO | 0.12 | 0.12 | 0.09 | 0.08 | 0.06 | 0.13 | 0.09 | 0.10 | 0.14 | 0.15 | 0.06 | 0.15 | 0.15 | 0.13 | 0.05 | 0.12 | 0.13 | 0.05 | 0.30 | 0.33 |
| MgO | 51.82 | 51.63 | 52.47 | 53.20 | 49.92 | 51.15 | 50.04 | 50.57 | 49.23 | 49.82 | 51.09 | 50.38 | 50.72 | 50.86 | 50.77 | 50.50 | 50.53 | 51.65 | 48.06 | 48.42 |
| CaO | 0.00 | 0.00 | 0.00 | 0.02 | 0.01 | 0.02 | 0.00 | 0.00 | 0.02 | 0.00 | 0.02 | 0.02 | 0.01 | 0.02 | 0.00 | 0.00 | 0.00 | 0.00 | 0.02 | 0.01 |
| $Na_2O$ | 0.00 | 0.00 | 0.01 | 0.00 | 0.00 | 0.00 | 0.04 | 0.05 | 0.00 | 0.02 | 0.00 | 0.01 | 0.00 | 0.00 | 0.00 | 0.00 | 0.00 | 0.00 | 0.00 | 0.08 |
| $K_2O$ | 0.01 | 0.02 | 0.04 | 0.01 | 0.01 | 0.00 | 0.01 | 0.02 | 0.00 | 0.00 | 0.01 | 0.00 | 0.00 | 0.00 | 0.01 | 0.00 | 0.00 | 0.02 | 0.00 | 0.01 |
| NiO | 0.36 | 0.34 | 0.34 | 0.36 | 0.34 | 0.32 | 0.31 | 0.35 | 0.22 | 0.34 | 0.38 | 0.39 | 0.36 | 0.30 | 0.35 | 0.27 | 0.37 | 0.38 | 0.19 | 0.20 |
| Totals | 99.87 | 100.26 | 99.72 | 100.18 | 99.46 | 100.91 | 99.44 | 100.35 | 99.12 | 99.27 | 100.27 | 99.41 | 99.59 | 100.02 | 100.26 | 99.95 | 99.52 | 100.56 | 100.07 | 100.28 |
| Si | 0.98 | 0.99 | 1.00 | 1.00 | 1.01 | 1.00 | 1.00 | 1.00 | 1.01 | 1.00 | 1.00 | 1.01 | 0.99 | 0.99 | 0.99 | 0.99 | 1.00 | 0.99 | 1.00 | 1.00 |
| Ti | 0.00 | 0.00 | 0.00 | 0.00 | 0.00 | 0.00 | 0.00 | 0.00 | 0.00 | 0.00 | 0.00 | 0.00 | 0.00 | 0.00 | 0.00 | 0.00 | 0.00 | 0.00 | 0.00 | 0.00 |
| Al | 0.00 | 0.00 | 0.00 | 0.00 | 0.00 | 0.00 | 0.00 | 0.00 | 0.00 | 0.00 | 0.00 | 0.00 | 0.00 | 0.00 | 0.00 | 0.00 | 0.00 | 0.00 | 0.00 | 0.00 |
| Cr | 0.00 | 0.00 | 0.00 | 0.00 | 0.00 | 0.00 | 0.00 | 0.01 | 0.00 | 0.00 | 0.00 | 0.00 | 0.00 | 0.00 | 0.00 | 0.00 | 0.00 | 0.00 | 0.00 | 0.00 |
| $Fe^{3+}$ | 0.02 | 0.02 | 0.01 | 0.00 | 0.00 | 0.01 | 0.00 | 0.00 | 0.00 | 0.01 | 0.00 | 0.00 | 0.02 | 0.02 | 0.02 | 0.02 | 0.01 | 0.02 | 0.00 | 0.01 |
| $Fe^{2+}$ | 0.14 | 0.14 | 0.11 | 0.10 | 0.17 | 0.16 | 0.17 | 0.16 | 0.18 | 0.17 | 0.15 | 0.15 | 0.15 | 0.15 | 0.16 | 0.16 | 0.16 | 0.14 | 0.23 | 0.21 |
| Mn | 0.00 | 0.00 | 0.00 | 0.00 | 0.00 | 0.00 | 0.00 | 0.00 | 0.00 | 0.00 | 0.00 | 0.00 | 0.00 | 0.00 | 0.00 | 0.00 | 0.00 | 0.00 | 0.01 | 0.01 |
| Mg | 1.88 | 1.86 | 1.88 | 1.90 | 1.82 | 1.84 | 1.82 | 1.83 | 1.80 | 1.82 | 1.84 | 1.83 | 1.85 | 1.84 | 1.84 | 1.84 | 1.84 | 1.86 | 1.77 | 1.77 |
| Ca | 0.00 | 0.00 | 0.00 | 0.00 | 0.00 | 0.00 | 0.00 | 0.00 | 0.00 | 0.00 | 0.00 | 0.00 | 0.00 | 0.00 | 0.00 | 0.00 | 0.00 | 0.00 | 0.00 | 0.00 |
| Na | 0.00 | 0.00 | 0.00 | 0.00 | 0.00 | 0.00 | 0.00 | 0.00 | 0.00 | 0.00 | 0.00 | 0.00 | 0.00 | 0.00 | 0.00 | 0.00 | 0.00 | 0.00 | 0.00 | 0.00 |
| K | 0.00 | 0.00 | 0.00 | 0.00 | 0.00 | 0.00 | 0.00 | 0.00 | 0.00 | 0.00 | 0.00 | 0.00 | 0.00 | 0.00 | 0.00 | 0.00 | 0.00 | 0.00 | 0.00 | 0.00 |
| Sum | 3.01 | 3.00 | 3.00 | 3.00 | 2.99 | 3.00 | 3.00 | 3.00 | 3.00 | 3.00 | 3.00 | 2.99 | 3.00 | 3.01 | 3.01 | 3.00 | 3.00 | 3.00 | 3.00 | 3.00 |
| $Fo^{\#}$ | 93.19 | 93.23 | 94.63 | 95.09 | 91.49 | 92.12 | 91.47 | 91.81 | 90.79 | 91.61 | 92.37 | 92.28 | 92.48 | 92.34 | 91.78 | 91.98 | 92.18 | 93.03 | 88.69 | 89.40 |

[a] Spinel-layered coarse-grained dunite.
[b] Spinel-poor coarse-grained dunite.

Green, 1980). However, three critical issues disfavor this inference. First, it is not possible to induce melting of the mantle at only 0.2 GPa (depth of ~6 km), because of the cold thermal boundary layer in extensional settings (e.g., mid-oceanic ridge and infant forearc). Second, the presence of spinel is obviously contradictory to the pressure condition of 0.2 GPa at which plagioclase is expected to be the stable aluminous phase. Third, assuming that spinel grains were formed purely by partial melting, the range of $Cr^{\#}$ (~76–84) in most spinel grains from harzburgite, coarse-grained and porphyroclastic dunite corresponds to over 30% fractional melting (Fig. 5e). Such extent of melting is obviously inconsistent with above estimated value (23–27% in fractional melting mode). Consequently, we consider that these high-$Cr^{\#}$ spinel grains ($spinel_3$) were not melting residues, but mainly formed during boninitic melt–rock reaction (boninite region in Fig. 5e). This explanation is also consistent with the frequent occurrence of euhedral spinel grains ($spinel_3$) in the coarse-grained dunite and harzburgite. Because the $Fo^{\#}$ in olivine is mainly controlled by the extent of melting and is insensitive to melting pressure (Fig. 5a), the olivine $Fo^{\#}$ of 91–93 can be formed either by partial melting ($olivine_2$) (e.g., 25–33% batch melting at the pressure much higher than 0.2 GPa) or by subsequent interaction with high-Mg boninitic magma ($olivine_3$).

Fourth, it is generally considered that the Ti content in spinel is mainly controlled by the composition of their equilibrium magmas or fluids (Arai, 1992; Kamenetsky et al., 2001). Hence the concentration of $TiO_2$ in spinel can be used to infer the chemical properties of reacting agents (Pearce et al., 2000). In coarse-grained dunite and harzburgite, the low but appreciable $TiO_2$ content (0.01–0.2 wt.%) of spinel grains thus suggests that these melting residues have subsequently interacted with a high-temperature magma which is poor in $TiO_2$ and rich in $Cr_2O_3$ and MgO (i.e. boninitic melt) (Fig. 5e):

$$Opx + Cpx + spinel_2 + melt_1 = olivine_3 + spinel_3 + melt_2 \quad (2)$$

where $melt_1$ is boninitic melt derived from high-degree partial melting (Eq. (1)), and $melt_2$ is the reacted boninitic melt richer in pyroxene components (modified from Pearce et al., 2000). The $spinel_2$ and $spinel_3$ thus indicate the original and newly-crystallized spinel during high-temperature melt–rock reactions.

Fifth, the presence of unusual oval and round multiphase inclusions in olivine and spinel grains (Figs. 3d and 4b–f) can suggest that the reacting melt was trapped by growing/crystallizing olivine and spinel crystals during melt–rock reaction (see section below).

Sixth, the melt–harzburgite reaction (consuming Opx of wall harzburgite) and subsequent mixing of melts (forming chromite-oversaturated melt) are essentially important to form dunite and chromitite in the mantle assemblage, respectively (e.g., Arai and Yurimoto, 1994; Melcher et al., 1997; Zhou et al., 1994, 1996). A sporadic occurrence of high-Cr banded chromitite and spinel-layered coarse-grained dunite in the Songshugou ultramafic massif (Figs. 1c and 2d), thus provides support for the melt–rock reaction interpretation. Specifically, the interlayering between spinel and olivine (Fig. 2d) is inferred to be originated from compaction, shearing and alternate crystallization of olivine and spinel from a mixed and segregated melt, resulting in the cumulate-like texture. Melt–rock reaction is used here as a general term to refer to the wide range of processes that can occur during melt transport in the mantle (Warren, 2016).

Seventh, the whole-rock compositions in MgO–$SiO_2$ and MgO–FeOt diagrams (Fig. 6c and d) indicate excess olivine in the harzburgites compared to that expected in partial melt residues. The excess olivine could have precipitated from the percolating melt through a post-melting process (e.g., Niu et al., 1997; Song et al., 2004).

### 6.3. Boninitic melt evidenced from multiphase inclusions

Because the host minerals can prevent fluids from escaping, the hydrous and carbonate phases in the multiphase inclusions can record the crystallization of volatile-rich melts or the reactions between trapped fluids and their host minerals. In contrast, anhydrous minerals (e.g., Opx, Cpx, and olivine) in multiphase inclusions are either likely nucleated from the trapped melt or captured as residual or nucleated crystals (Li et al., 2005; Matsukage and Arai, 1998). In this study, we observed two major hydrous minerals within inclusions. One is Cr-chlorite

**Table 2**
Representative composition of spinel.

| Rock type | Coarse-grained dunite | | | | | | | | Porphyroclastic dunite | | | | Fine-grained dunite | | | | Harzburgite | | Olivine clinopyroxenite | |
|---|---|---|---|---|---|---|---|---|---|---|---|---|---|---|---|---|---|---|---|---|
| Sample | SSG-2[a] | | S95-31[a] | | S03-2A[b] | | S03-2C[b] | | S91-26 | | SSG-1 | | S91-03 | | S91-05 | | S03-2B | | S91-32 | |
| $SiO_2$ | 0.00 | 0.01 | 0.00 | 0.00 | 0.05 | 0.04 | 0.00 | 0.00 | 0.02 | 0.01 | 0.00 | 0.06 | 0.00 | 0.05 | 0.01 | 0.05 | 0.04 | 0.03 | 0.00 | 0.00 |
| $TiO_2$ | 0.13 | 0.10 | 0.11 | 0.05 | 0.10 | 0.07 | 0.03 | 0.03 | 0.08 | 0.11 | 0.07 | 0.04 | 0.68 | 0.59 | 0.35 | 0.25 | 0.03 | 0.00 | 0.39 | 0.47 |
| $Al_2O_3$ | 10.01 | 10.51 | 9.30 | 9.24 | 8.41 | 9.70 | 8.99 | 8.37 | 6.06 | 2.15 | 7.60 | 2.60 | 1.24 | 1.29 | 5.25 | 3.40 | 9.56 | 9.50 | 0.99 | 1.07 |
| $Cr_2O_3$ | 53.19 | 53.99 | 57.51 | 57.67 | 52.85 | 52.54 | 52.59 | 51.12 | 41.08 | 44.61 | 56.67 | 63.03 | 32.33 | 34.25 | 45.59 | 49.93 | 55.11 | 55.77 | 27.34 | 28.66 |
| $Fe_2O_3$ | 7.01 | 6.20 | 6.36 | 6.12 | 7.14 | 6.74 | 8.28 | 9.49 | 20.54 | 20.62 | 5.02 | 3.80 | 34.94 | 33.27 | 18.16 | 16.08 | 5.50 | 4.77 | 41.36 | 39.95 |
| FeO | 21.70 | 22.04 | 15.16 | 15.98 | 23.05 | 22.70 | 22.73 | 23.75 | 25.34 | 26.26 | 22.02 | 22.75 | 28.23 | 27.25 | 25.74 | 25.26 | 22.93 | 22.94 | 27.44 | 28.03 |
| MnO | 0.42 | 0.41 | 0.38 | 0.33 | 0.43 | 0.37 | 0.42 | 0.40 | 0.57 | 0.63 | 0.49 | 0.48 | 0.51 | 0.40 | 0.57 | 0.56 | 0.42 | 0.40 | 0.66 | 0.72 |
| MgO | 7.52 | 7.34 | 11.71 | 11.36 | 6.13 | 6.54 | 6.25 | 5.67 | 3.51 | 2.77 | 6.51 | 5.31 | 2.41 | 3.01 | 4.35 | 4.33 | 6.73 | 6.63 | 2.43 | 2.43 |
| CaO | 0.00 | 0.03 | 0.00 | 0.04 | 0.00 | 0.03 | 0.00 | 0.02 | 0.02 | 0.04 | 0.00 | 0.03 | 0.00 | 0.01 | 0.00 | 0.02 | 0.00 | 0.00 | 0.02 | 0.02 |
| $Na_2O$ | 0.01 | 0.06 | 0.06 | 0.00 | 0.00 | 0.02 | 0.11 | 0.01 | 0.16 | 0.03 | 0.07 | 0.12 | 0.01 | 0.03 | 0.00 | 0.04 | 0.01 | 0.02 | 0.08 | 0.00 |
| $K_2O$ | 0.00 | 0.00 | 0.01 | 0.00 | 0.00 | 0.01 | 0.01 | 0.01 | 0.00 | 0.01 | 0.00 | 0.03 | 0.00 | 0.01 | 0.00 | 0.00 | 0.00 | 0.00 | 0.00 | 0.00 |
| NiO | 0.00 | 0.00 | 0.04 | 0.07 | 0.00 | 0.02 | 0.05 | 0.01 | 0.17 | 0.12 | 0.05 | 0.04 | 0.37 | 0.41 | 0.06 | 0.10 | 0.07 | 0.00 | 0.26 | 0.21 |
| Totals | 99.99 | 100.69 | 100.64 | 100.86 | 98.16 | 98.75 | 99.41 | 98.87 | 97.38 | 97.25 | 98.45 | 98.25 | 100.72 | 100.57 | 100.08 | 100.02 | 100.40 | 100.06 | 100.97 | 101.56 |
| Si | 0.00 | 0.00 | 0.00 | 0.00 | 0.00 | 0.00 | 0.00 | 0.00 | 0.00 | 0.00 | 0.00 | 0.00 | 0.00 | 0.00 | 0.00 | 0.00 | 0.00 | 0.00 | 0.00 | 0.00 |
| Ti | 0.00 | 0.00 | 0.00 | 0.00 | 0.00 | 0.00 | 0.00 | 0.00 | 0.00 | 0.00 | 0.00 | 0.00 | 0.02 | 0.02 | 0.01 | 0.01 | 0.00 | 0.00 | 0.01 | 0.01 |
| Al | 0.40 | 0.41 | 0.36 | 0.36 | 0.35 | 0.39 | 0.36 | 0.34 | 0.26 | 0.10 | 0.31 | 0.11 | 0.05 | 0.06 | 0.22 | 0.14 | 0.38 | 0.38 | 0.04 | 0.05 |
| Cr | 1.42 | 1.43 | 1.49 | 1.49 | 1.46 | 1.43 | 1.43 | 1.41 | 1.18 | 1.32 | 1.56 | 1.79 | 0.94 | 0.99 | 1.28 | 1.41 | 1.48 | 1.50 | 0.80 | 0.83 |
| $Fe^{3+}$ | 0.18 | 0.16 | 0.16 | 0.15 | 0.19 | 0.17 | 0.21 | 0.25 | 0.56 | 0.58 | 0.13 | 0.10 | 0.97 | 0.92 | 0.48 | 0.43 | 0.14 | 0.12 | 1.15 | 1.10 |
| $Fe^{2+}$ | 0.61 | 0.62 | 0.41 | 0.44 | 0.67 | 0.65 | 0.65 | 0.69 | 0.77 | 0.82 | 0.64 | 0.68 | 0.87 | 0.84 | 0.76 | 0.76 | 0.65 | 0.65 | 0.85 | 0.86 |
| Mn | 0.01 | 0.01 | 0.01 | 0.01 | 0.01 | 0.01 | 0.01 | 0.01 | 0.02 | 0.02 | 0.01 | 0.02 | 0.02 | 0.01 | 0.02 | 0.02 | 0.01 | 0.01 | 0.02 | 0.02 |
| Mg | 0.38 | 0.37 | 0.57 | 0.55 | 0.32 | 0.34 | 0.32 | 0.29 | 0.19 | 0.16 | 0.34 | 0.28 | 0.13 | 0.16 | 0.23 | 0.23 | 0.34 | 0.34 | 0.13 | 0.13 |
| Ca | 0.00 | 0.00 | 0.00 | 0.00 | 0.00 | 0.00 | 0.00 | 0.00 | 0.00 | 0.00 | 0.00 | 0.00 | 0.00 | 0.00 | 0.00 | 0.00 | 0.00 | 0.00 | 0.00 | 0.00 |
| Na | 0.00 | 0.00 | 0.00 | 0.00 | 0.00 | 0.00 | 0.01 | 0.00 | 0.01 | 0.00 | 0.01 | 0.01 | 0.00 | 0.00 | 0.00 | 0.00 | 0.00 | 0.00 | 0.01 | 0.00 |
| K | 0.00 | 0.00 | 0.00 | 0.00 | 0.00 | 0.00 | 0.00 | 0.00 | 0.00 | 0.00 | 0.00 | 0.00 | 0.00 | 0.00 | 0.00 | 0.00 | 0.00 | 0.00 | 0.00 | 0.00 |
| Sum | 3.00 | 3.00 | 3.00 | 3.00 | 3.00 | 3.00 | 3.00 | 3.00 | 3.00 | 3.00 | 3.00 | 3.00 | 3.00 | 3.00 | 3.00 | 3.00 | 3.00 | 3.00 | 3.00 | 3.00 |
| $Cr^{\#}$ | 78.08 | 77.52 | 80.58 | 80.73 | 80.82 | 78.42 | 79.69 | 80.35 | 81.97 | 93.29 | 83.32 | 94.21 | 94.57 | 94.66 | 85.36 | 90.79 | 79.43 | 79.75 | 94.87 | 94.74 |
| $X_{Cr}$ | 0.71 | 0.71 | 0.74 | 0.75 | 0.73 | 0.71 | 0.71 | 0.70 | 0.59 | 0.66 | 0.78 | 0.90 | 0.47 | 0.50 | 0.64 | 0.71 | 0.74 | 0.75 | 0.40 | 0.41 |
| $X(Fe^{2+})$ | 0.62 | 0.63 | 0.42 | 0.44 | 0.68 | 0.66 | 0.67 | 0.70 | 0.80 | 0.84 | 0.66 | 0.71 | 0.87 | 0.84 | 0.77 | 0.77 | 0.66 | 0.66 | 0.86 | 0.87 |
| $Y(Fe^{3+})$ | 0.09 | 0.08 | 0.08 | 0.08 | 0.09 | 0.09 | 0.11 | 0.12 | 0.28 | 0.29 | 0.07 | 0.05 | 0.49 | 0.47 | 0.24 | 0.22 | 0.07 | 0.06 | 0.58 | 0.56 |

$Cr^{\#} = 100 * Cr/(Cr + Al)$; $X_{Cr} = Cr/(Cr + Al + Fe^{3+})$; $X(Fe^{2+}) = Fe^{2+}/(Fe^{2+} + Mg)$; $Y(Fe^{3+}) = Fe^{3+}/(Fe^{3+} + Cr + Al)$.

[a] Spinel-layered coarse-grained dunite.

[b] Spinel-poor coarse-grained dunite.

**Table 3**
Representative compositions of multiphase inclusions.

| Rock type | Coarse -grained dunite | | | | | | | | | | | | | Fine -grained dunite | | | | | | Harzburgite | | |
|---|---|---|---|---|---|---|---|---|---|---|---|---|---|---|---|---|---|---|---|---|---|---|
| Sample | S-15[a] | | SSG-2[a] | | | | | S-11[b] | | | S03-2C[b] | | | S-05 | | | | | | S-249 | | S03-2B |
| $SiO_2$ | 35.14 | 42.88 | 56.38 | 30.49 | 0.06 | 56.68 | 36.03 | 57.81 | 39.06 | 39.62 | 58.98 | 32.38 | 31.17 | 1.34 | 45.32 | 35.98 | 41.93 | 10.40 | 38.86 | 33.28 | 40.86 | 58.36 |
| $TiO_2$ | 0.03 | 0.03 | 0.01 | 0.03 | 0.05 | 0.00 | 0.00 | 0.00 | 0.00 | 0.00 | 0.00 | 0.09 | 0.00 | 0.03 | 0.05 | 0 02 | 0.03 | 0.06 | 0.04 | 0.00 | 0.00 | 0.00 |
| $Al_2O_3$ | 9.54 | 0.73 | 1.20 | 16.54 | 0.03 | 0.71 | 10.48 | 0.12 | 3.72 | 0.06 | 0.09 | 15.24 | 16.11 | 0.11 | 0.66 | 10.64 | 0.05 | 0.00 | 0.02 | 15.07 | 0.06 | 0.26 |
| $Cr_2O_3$ | 1.76 | 0.05 | 0.81 | 2.61 | 0.49 | 0.14 | 2.00 | 0.36 | 1.66 | 0.08 | 0.20 | 3.13 | 2.73 | 0.84 | 0.11 | 2.02 | 0.15 | 0.14 | 0.97 | 1.29 | 0.03 | 0.04 |
| FeO | 4.57 | 8.65 | 1.35 | 1.94 | 0.99 | 1.34 | 3.89 | 1.39 | 7.73 | 9.63 | 5.82 | 2.51 | 1.99 | 85.99 | 5.43 | 4.15 | 8.53 | 4.96 | 5.91 | 3.64 | 8.25 | 5.57 |
| MnO | 0.06 | 0.01 | 0.03 | 0.02 | 0.08 | 0.07 | 0.03 | 0.03 | 0.07 | 0.18 | 0.17 | 0.05 | 0.03 | 0.07 | 0.12 | 0.06 | 0.16 | 0.31 | 0.13 | 0.05 | 0.16 | 0.14 |
| NiO | 0.24 | 0.12 | 0.00 | 0.28 | 0.01 | 0.00 | 0.25 | 0.19 | 0.30 | 0.34 | 0.00 | 0.19 | 0.14 | 0.94 | 0.23 | 0.22 | 0.31 | 0.03 | 0.24 | 0.13 | 0.16 | 0.07 |
| MgO | 38.24 | 45.52 | 23.21 | 32.15 | 23.62 | 23.26 | 39.19 | 27.77 | 42.55 | 47.79 | 35.57 | 33.17 | 32.65 | 4.61 | 44.08 | 33.20 | 48.25 | 44.49 | 44.35 | 33.34 | 49.21 | 35.67 |
| CaO | 0.02 | 0.00 | 13.81 | 0.05 | 32.06 | 13.89 | 0.00 | 0.05 | 0.05 | 0.00 | 0.02 | 0.00 | 0.00 | 0.06 | 0.00 | 0.05 | 0.00 | 0.10 | 0.02 | 0.00 | 0.01 | 0.07 |
| $Na_2O$ | 0.00 | 0.02 | 0.23 | 0.01 | 0.00 | 0.56 | 0.01 | 0.06 | 0.00 | 0.03 | 0.11 | 0.00 | 0.00 | 0.06 | 0.02 | 0.06 | 0.00 | 0.03 | 0.00 | 0.00 | 0.00 | 0.00 |
| $K_2O$ | 0.00 | 0.03 | 0.03 | 0.01 | 0.04 | 0.00 | 0.01 | 0.00 | 0.00 | 0.00 | 0.01 | 0.00 | 0.01 | 0.00 | 0.00 | 0.00 | 0.00 | 0.00 | 0.00 | 0.00 | 0.00 | 0.01 |
| Total | 89.61 | 98.05 | 97.06 | 84.13 | 57.43 | 96.65 | 91.89 | 87.78 | 95.14 | 97.73 | 100.96 | 86.76 | 84.83 | 94.05 | 96.03 | 86.33 | 99.40 | 60.52 | 90.55 | 86.82 | 98.73 | 100.18 |
| $Mg^{\#}$ | 0.94 | 0.90 | 0.97 | 0.97 | | 0.97 | 0.97 | 0.97 | 0.91 | 0.90 | 0.92 | 0.96 | 0.96 | | 0.94 | 0.94 | 0.91 | | 0.93 | 0.94 | 0.91 | 0.91 |
| $Cr^{\#}$ | 0.11 | | | 0.10 | | 0.10 | 0.12 | | 0.23 | | | 0.12 | 0.12 | | | 0.11 | | | | 0.05 | | |
| Mineral phase | Chl | Ol | Tr | Chl | Dol | Tr[c] | Chl[d] | Opx? | Ol/Chl? | Ol | Opx | Chl | Chl[c] | Mag | Ol | Chl | Ol | Mgs | Ol? | Chl | Ol | Opx[c] |

[a] Spinel-layered coarse-grained dunite; [b] Spinel-poor coarse-grained dunite
[c] Mineral in matrix; [d] Monophase inclusion
Abbreviation: olivine (Ol), orthopyroxene (Opx), chlorite (Chl), tremolite (Tr), magnetite (Mag), magnesite (Mgs), dolomite (Dol)

that is characterized by higher MgO, $Cr_2O_3$, and $Al_2O_3$ contents, and the other is tremolite, which has higher $SiO_2$ and CaO contents. Both of them are poor in incompatible elements such as $TiO_2$, $Na_2O$, and $K_2O$ (Table 3). The chemical compositions of tremolite and Cr-chlorite in the multiphase inclusions resemble those of their matrix counterparts (Table 3), implying that these multiphase inclusions may be the artifact of retrograde hydration reactions (see discussion below). However, their unusual and perfect oval or round shapes, and lacking obvious cracks connecting with the matrix favors the genesis of multiphase inclusions as trapped melts (Figs. 3d and 4b–f). Therefore, the multiphase inclusions (Figs. 3d and 4b–f; especially those included in silica-free spinel) suggest that the trapped melt probably had a close relationship with reacting hydrous boninitic magmas (i.e. $melt_{1,2}$ in Eq. (2)), which was most likely captured by (re)crystallizing olivine ($olivine_3$) and spinel ($spinel_3$) during high-temperature boninitic melt–rock reaction (Eq. (2)). This high temperature inference is also consistent with the estimated high homogenization temperatures (~1200–1300 °C) for these multiphase inclusions (Su et al., 2005). The reasons for the varying mineral species, compositions and volume proportions residing in multiphase inclusions are puzzling, which may be due to the compositional heterogeneity of the boninitic melt in the system or to the post-entrapment reactions between trapped melts and their host minerals (Li et al., 2005; Matsukage and Arai, 1998).

Together with the occurrences of carbonate minerals (e.g., dolomite and magnesite) in both types of multiphase inclusions, it is suggested that, besides water, the trapped melt was also rich in $CO_2$. In addition, the occurrence of magnetite (Fig. 4e) in the multiphase inclusions may imply that a fair amount of oxidation by the trapped melt, indicative of the high oxygen fugacity in the forearc mantle. These characteristics of multiphase inclusions thus point to an intimate association with fluid-rich (i.e. $H_2O$ and $CO_2$) boninitic magma in a forearc mantle setting (see section below).

Different from the results in this study, many previous studies discovered multiphase hydrous inclusions of amphibole (mostly Na-, Ti-pargasite) and phlogopite in spinel (chromite) of mafic intrusions and ultramafic alkaline complex (e.g., Li et al., 2005; Lorand and Cottin, 1987; Renna and Tribuzio, 2011; Spandler et al., 2005; Tian et al., 2011; Veksler et al., 1998). Because of the compositional similarities between inclusion and matrix phases of tremolite and Cr-chlorite, and lack of experimental data supporting their magmatic origins, it raises the possibility that these multiphase inclusions may also represent matrix fragments (i.e. metamorphic origin) that were incorporated during the solid-state growth of the host phase olivine and spinel, which requires a more complex petrological history of Songshugou peridotites. However, this interpretation of metamorphic origin of multiphase inclusions may suffer difficulties such as in explaining the high $Cr^{\#}$ in spinel (i.e. chromite which is generally considered magmatic origin) by decomposing the lower $Cr^{\#}$ chlorite in the matrix without forming other extremely $Al_2O_3$ rich phases. In fact, the lower $Cr^{\#}$ chlorite in the matrix was most likely produced by the breakdown of moderate $Cr^{\#}$ spinel with accompanied growth of higher $Cr^{\#}$ spinel (see Section 6.5.2). Besides, the spatially sporadic distribution and fairly homogenous composition of multiphase inclusion bearing spinel—the occurrence of spinel displaying patchy composition pattern (Fig. 3c) indicate that the diffusion of some elements in spinel may not be that efficient—may also disfavor the interpretation of solid-state recrystallization, conglomerating and annealing of neighboring spinel grains in a matrix consisting of hydrous phases (Lorand and Cottin, 1987). The absence of carbonite in the matrix might reflect the dissolution of carbonate by injected fluids during subsequent fluid–rock reactions at low or sub-solidus temperatures (Ague and Nicolescu, 2014; Poli, 2015), whereas carbonate can be well protected and preserved as inclusions in olivine and spinel. Therefore, even though the multiphase hydrous inclusions of tremolite and Cr-chlorite such as in this study are rarely observed, we cannot rule out their possible origin as trapped magma.

A key reason that may account for the presence of Na-, Ti-pargasite and phlogopite multiphase inclusions in other's studies (e.g., Li et al., 2005; Lorand and Cottin, 1987; Renna and Tribuzio, 2011; Spandler et al., 2005; Tian et al., 2011; Veksler et al., 1998) is that the melt could be more fertile or evolved (thus richer in alkalis and titanium), since these inclusions were almost found in mafic intrusions and ultramafic alkaline complex. On the contrary, the tremolite and Cr-chlorite multiphase inclusions in our study are associated with refractory ultramafic peridotites, and are thus potentially indicative of a depleted melt (i.e. boninite). Albeit absent of tremolite and Cr-chlorite, the depleted

composition of primitive melt was recently reported in the spinel-hosted melt inclusions (52–63 wt.% $SiO_2$, 7–23 wt.% MgO, and 0.01–0.25 wt.% $TiO_2$) in boninite from the Ogasawara Archipelago in Japan (Umino et al., 2015). To confirm the magmatic origin of tremolite and Cr-chlorite, further experimental studies on the crystallizing products (i.e. liquid phases) of hydrous boninitic melt at various physico-chemical conditions are needed.

### 6.4. Origin of olivine clinopyroxenite

Several field and petrographic arguments illustrate that the olivine clinopyroxenite (similar to wehrlite) is a typical crystallization product from a primitive magma or via interactions with silica-saturated melts with high melt/rock ratios, as indicated by the high modal abundance of clinopyroxene megacrysts (Fig. 2f) and dyke occurrences in the field (Su et al., 2005). The olivine clinopyroxenite displays contrastingly lower olivine modal abundance (~30–35%) and MgO content or whole-rock $Mg^{\#}$ (~87–91) than most harzburgite and dunite (Fig. 6b–f). The depleted LREEs, flat and enriched MREE–HREEs (0.5–1 times chondrite) pattern in olivine clinopyroxenite (Fig. 7e) are also obviously different from those of dunite and harzburgite (Fig. 7a–d). Besides, the $Fo^{\#}$ in olivine clinopyroxenite varies in a continuous range of 84–90, which is lower than the olivine in dunite and harzburgite (Fig. 5a and b), whereas the contents of $Fe^{2+}$, $Fe^{3+}$, and $TiO_2$ in spinel are similar to those of fine-grained dunite (Fig. 5c–f). The continuous variations of olivine and spinel compositions in olivine clinopyroxenite can most properly be explained by a compositional change during fractional crystallization of magma and/or its successive reactions with wall-rocks in the course of dyke growth. This chemically relatively fertile magma (Cpx-saturated; richer in Si, Fe, and Ti; poorer in Mg and Cr) is likely derived from successive fractionation events and/or melt–rock reactions (starting from the high-T boninitic melt–rock reaction) (Kelemen et al., 1992). It is noteworthy that the olivine in olivine clinopyroxenite has a relatively lower $Fo^{\#}$ than the olivine in dunite and harzburgite, and its continuous $Fo^{\#}$ variation between 84 and 90 is likely indicative of a slight magma evolution. However, this olivine $Fo^{\#}$ (84–90) is still high enough to suggest a primitive origin. This result is consistent with the $Fo^{\#}$ range in the olivine precipitated from most primitive basalts on the Earth. Distinct from the crystallization of tremolite (i.e. magmatic origin) in multiphase inclusions (i.e. a closed system; Figs. 3d and 4c) where fluid can be preserved, the crystallization of anhydrous Cpx and olivine in olivine clinopyroxenite suggests that the residual hydrous melt (or fluids) likely escaped from the open system. Actually, olivine clinopyroxenite is equivalent to wehrlite cumulates resulting from fractional crystallization of hydrous basaltic melts (Gaetani and Grove, 1998; Niu, 2005) or from less hydrous magmas under high pressures (>8 kbar) (see Niu (2005) for a summary).

Following an intermediate stage of magma evolution from olivine- to Cpx-saturated compositions that is coupled with multistage melt–rock reactions, an Opx-saturated melt is expected (Kelemen et al., 1992). This Opx-saturated melt is capable of crystallizing more Opx than olivine during melt–rock reaction, and thus results in a cumulate-like harzburgite texture rather than a residual harzburgite. This melt–rock reaction process may be evidenced by a few Opx-rich harzburgite samples that have mineral modes and major-element compositions that significantly deviate from the main trends of most dunite–harzburgite sequences (Fig. 6a–f).

### 6.5. Low-temperature fluid–rock reactions

#### 6.5.1. $TiO_2$-rich fluid–rock reaction

As shown in Fig. 5e, the spinel grains in fine-grained dunite have contrastingly higher $TiO_2$ content than those in coarse-grained dunite and harzburgite. The fine-grained dunite has similarly high olivine $Fo^{\#}$ (~91–93) as coarse-grained dunite and harzburgite, this fact implies that the reacting agent is not likely a tholeiitic magma that is rich in $SiO_2$, FeO, and $TiO_2$ and poor in MgO, because reaction with a tholeiitic melt would produce significantly lower $Fo^{\#}$ olivine which however was not observed in fine-grained dunite. Instead, the fine-grained dunite likely results from the modification of spinel compositions in their coarse-grained counterparts through a later interaction with a low-T $TiO_2$-rich aqueous fluid (Fig. 5e):

$$\text{spinel}_3 + \text{TiO}_2\text{-rich fluid} = \text{spinel}_4 \quad (3)$$

where $spinel_3$ and $spinel_4$ are poor and rich in $TiO_2$, respectively. Texturally, this hydrothermal reaction process is supposed to alter the original shape of spinel, which is consistent with the strongly fractured spinel grains in fine-grained dunite (Fig. 3a). The conventionally believed fluid-immobile $TiO_2$ can become dramatically soluble and mobile in a chloride- and fluoride-bearing aqueous fluid under relatively high temperatures of ~900–1100 °C (e.g., Ayers and Watson, 1993; Rapp et al., 2010). To prove this hypothesis of participation of chloride- or fluride-bearing fluids, more detailed analyses and comparisons of other trace-element abundances in spinel from coarse- and fine-grained dunites are needed.

#### 6.5.2. Cr-chlorite-forming fluid–rock reaction

Cr-chlorite is a hydrous phase that is ubiquitously observed in our studied peridotite samples and other ultramafic rocks (e.g., Merlini et al., 2009). Because the thermodynamic properties of most Cr-bearing minerals are not known, the precise P–T stability field of Cr-chlorite in ultramafic rocks cannot be modeled using phase equilibria diagrams. However, a few recent experimental studies suggested that the chromium-bearing chlorite is more stable than chromium-free chlorite; and it can persist to higher P–T condition at ~900 °C at 3.5 GPa (Fischer et al., 2008).

In our studied peridotites, the occurrence of Cr-chlorite in the cleavages, fractures and near Cr-rich spinel (Figs. 3a, b, and 4f) imply that the spinel is altered through a chlorite-forming reaction (modified after Kimball (1990)):

$$2\ \underset{\text{spinel}_4}{\text{Mg(Al, Cr)}_2\text{O}_4} + \underset{\text{forsterite}}{\text{Mg}_2\text{SiO}_4} + \underset{\text{enstatite}}{\text{Mg}_2\text{Si}_2\text{O}_6} + 4\text{H}_2\text{O} = \underset{\text{chlorite}}{\text{Mg}_5\text{(Al, Cr)}_2\text{Si}_3\text{O}_{10}\text{(OH)}_8} + \underset{\text{spinel}_5}{\text{Mg(Cr, Al)}_2\text{O}_4} \quad (4)$$

through which Mg, Al and Cr in spinel can be transferred to form chlorite. Because chlorite has a much lower $Cr^{\#}$ (i.e. higher Al/Cr ratio) than spinel, the formation of chlorite will extract more $Al_2O_3$ than $Cr_2O_3$ from spinel ($spinel_4$) and result in a higher $Cr^{\#}$ in the altered spinel crystals ($spinel_5$) (Fig. 5e). Therefore, the higher $Cr^{\#}$ and $TiO_2$ contents of spinel in fine-grained dunite compared with coarse-grained dunite and harzburgite (Fig. 5a, e and f), could be due to more intensive fluid–rock interactions and formation of chlorite experienced by the fine-grained dunite compared to the other rocks (Fig. 3). Based on the mass balance calculation between the average $Cr^{\#}$ of Cr-chlorite

**Fig. 6.** (a) Recalculated normative Ol–Opx–Cpx modes of peridotites using their whole-rock major element compositions and CIPW norm (see Niu, 1997). (b) Relationship between the recalculated modal proportion of olivine and the whole-rock Mg number. (c–f) Diagrams showing the whole-rock MgO content vs. other oxides content (wt.%). (c) MgO vs. $SiO_2$, (d) MgO vs. FeOt, (e) MgO vs. $Al_2O_3$, and (f) MgO vs. CaO. The variations of $SiO_2$, FeOt, and MgO contents in the melting residue from a fertile MORB mantle (FMM) source are calculated in three different melting models and are displayed in diagram (c) and (d). Three different melting models: one is near-fractional decompression melting from 25 to 8 kbar, and the other two are isobaric batch melting at 10 and 20 kbar. Shading regions in (c) and (d) are the olivine compositions in Songshugou dunite and harzburgite. The deviations of two harzburgite samples from the main trends in (e) and (f) are likely attributed to their high modal abundance of Opx. (f) One harzburgite sample has a significantly higher CaO content (3.44 wt.%) than other harzburgite and dunite samples, possibly owing to the enrichment of carbonate minerals. (c) and (d) Modified after Niu (1997).

(~10), unaltered (~80) and altered (~95) spinel, about 20% mass of spinel is needed to be chloritized to explain the observed $Cr^{\#}$ in chlorite and spinel. Because the reacted residual boninitic melt is rich in $TiO_2$ and the dyke structure can provide an effective path for fluid flow, olivine clinopyroxenite also tends to have a similarly higher $Cr^{\#}$ and $TiO_2$ contents of spinel by facilitating the chlorite-forming reactions (Fig. 5e).

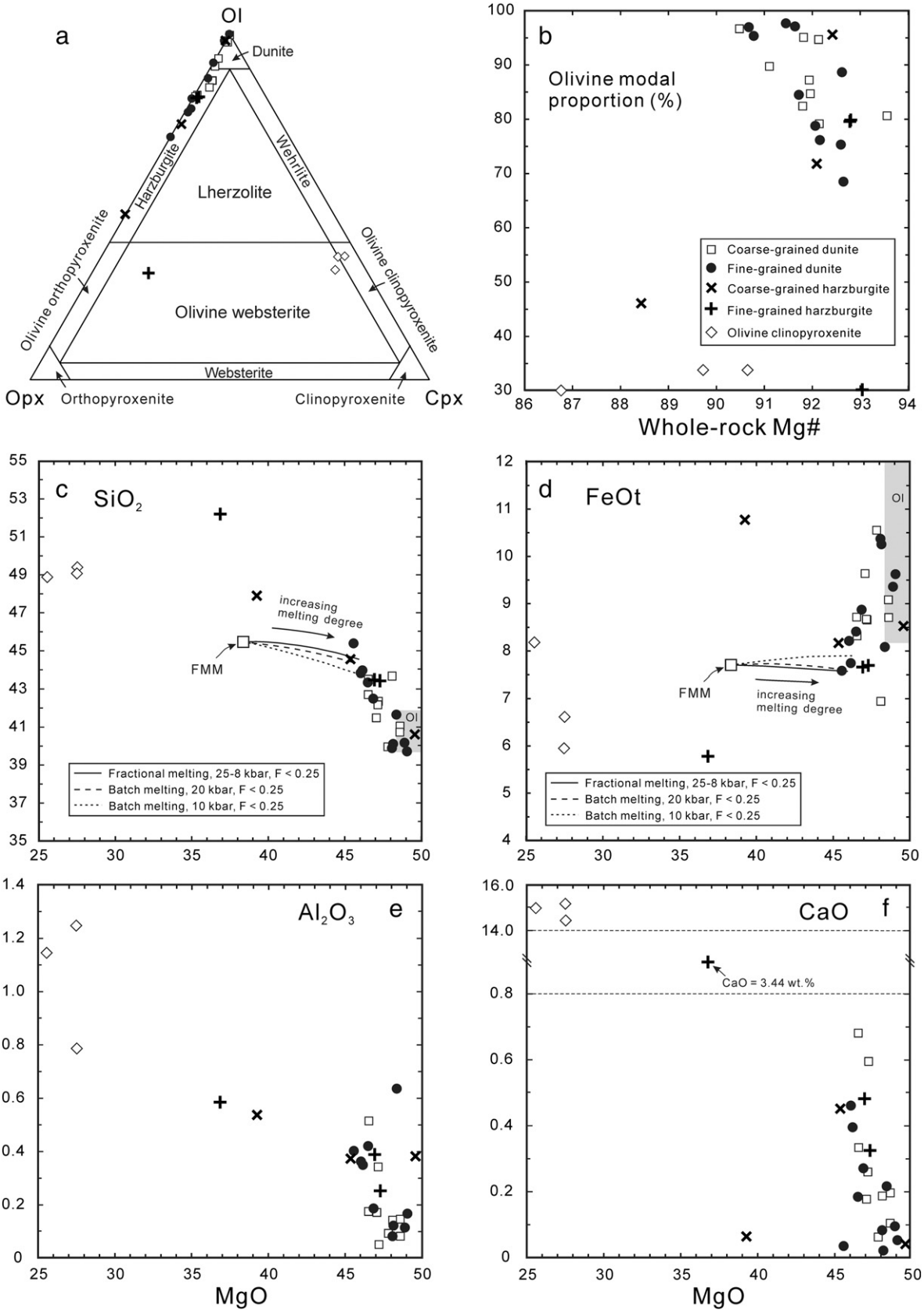

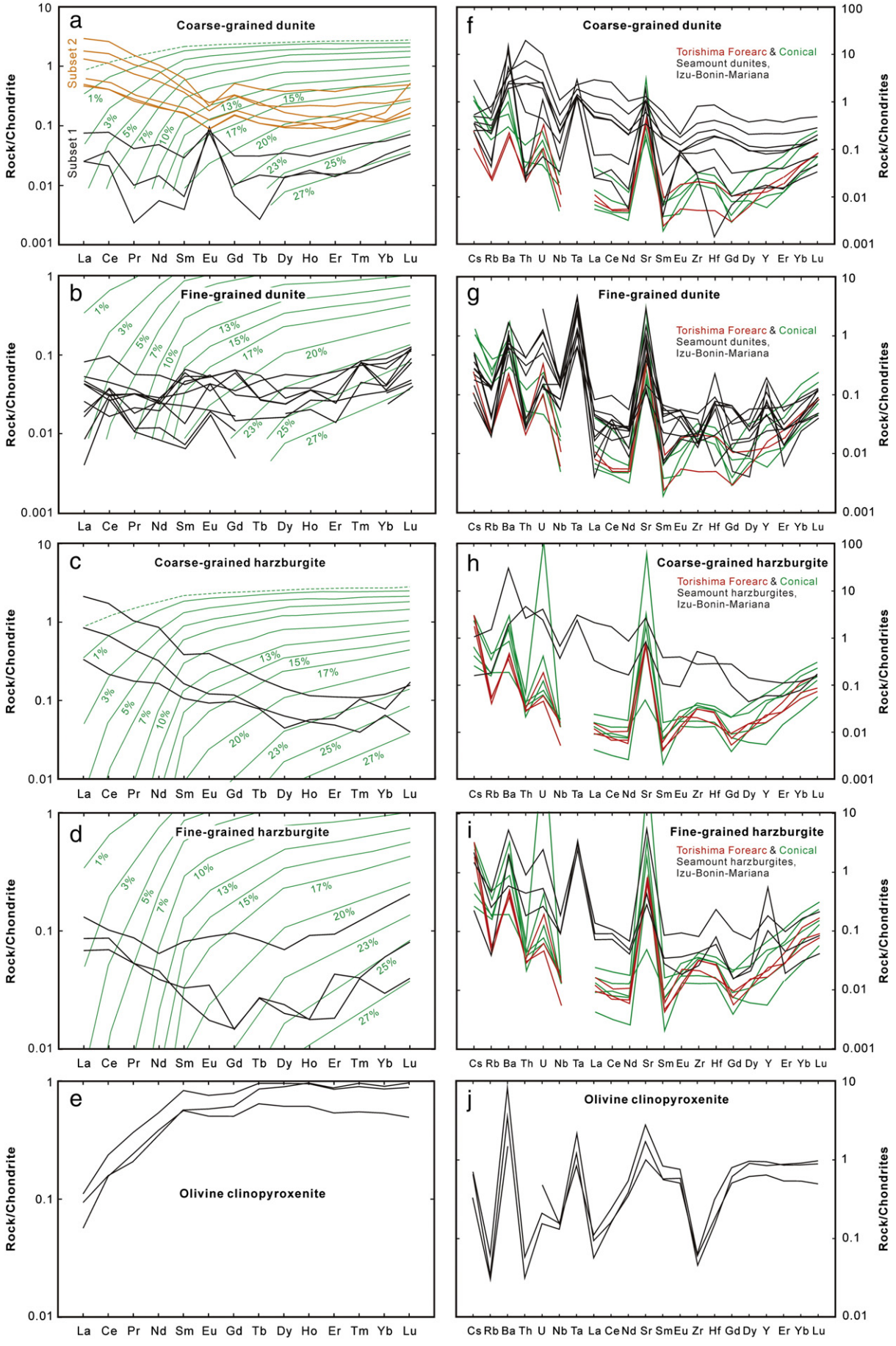
a
Coarse-grained dunite
Subset 2
Subset 1
1%
3%
5%
7%
10%
13%
15%
17%
20%
23%
25%
27%
Rock/Chondrite
La Ce Pr Nd Sm Eu Gd Tb Dy Ho Er Tm Yb Lu
f
Coarse-grained dunite
Torishima Forearc & Conical Seamount dunites, Izu-Bonin-Mariana
Rock/Chondrites
Cs Rb Ba Th U Nb Ta La Ce Nd Sr Sm Eu Zr Hf Gd Dy Y Er Yb Lu
b
Fine-grained dunite
g
Fine-grained dunite
c
Coarse-grained harzburgite
h
Coarse-grained harzburgite
Torishima Forearc & Conical Seamount harzburgites, Izu-Bonin-Mariana
d
Fine-grained harzburgite
i
Fine-grained harzburgite
e
Olivine clinopyroxenite
j
Olivine clinopyroxenite

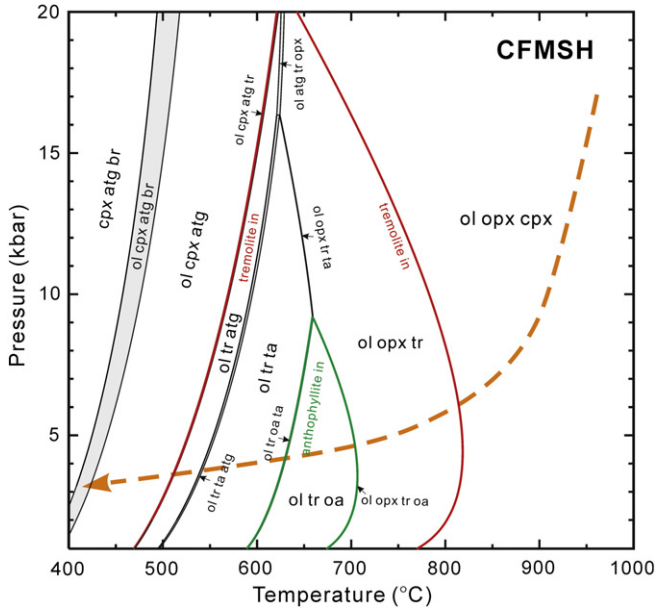


**Fig. 8.** P–T pseudosection for a representative coarse-grained dunite in the system CFMSH (modal proportions of oxides: CaO = 0.60, FeO = 6.49, MgO = 57.25, $SiO_2$ = 35.25, $H_2O$ in excess), calculated using THERMOCALC v3.33 (Powell et al., 1998). Green and red lines indicate the stability field of ortho-amphibole and tremolite, respectively. Yellow dashed arrowed is an assumed exhumation P–T path. Mineral abbreviation: antigorite (atg), brucite (br), clinopyroxene (cpx), ortho-amphibole (oa), olivine (ol), ortho-amphibole (oa), orthopyroxene (opx), talc (ta), and tremolite (tr). (For interpretation of the references to color in this figure legend, the reader is referred to the web version of this article.)

*6.5.3. Amphibole-forming fluid–rock reaction*

This low-T fluid rock reaction can be represented as hydration reaction resulting in the ubiquitous occurrence of amphibole minerals (i.e. anthophyllite and tremolite) in the matrix (Figs. 2, 3a and 4d) or monophase inclusions in olivine and Opx (representing healed cracks) (Figs. 2e, 4a and e). As shown in the P–T pseudosection, the dominant amphibole phase, anthophyllite is stable at a pressure lower than 1 GPa and a temperature of 600–700 °C (Fig. 8; see also Yang and Powell, 2008). This P–T condition hinders the prevalence of plastic deformation of peridotite, but favors brittle microcracking (with lack of displacement), which can explain why large euhedral amphibole grains crosscut olivine crystals in all dunite samples (Fig. 2a–e). A detailed phase reaction analysis using THERMOCALC suggests that ortho-amphibole (i.e. anthophyllite) was mostly formed by consuming Opx:

$$9\underset{\text{Opx}}{(Mg,Fe)_2SiO_6} + 2H_2O = \underset{\text{ortho-amphibole}}{2(Mg,Fe)_7Si_8O_{22}(OH)_2} + 2\underset{\text{olivine}_4}{(Mg,Fe)_2SiO_4}\,. \quad (5)$$

Namely, 2 mol of ortho-amphibole and 2 mol of olivine are produced by reacting 9 mol of Opx with water. In the studied dunite, the volume proportion of amphibole (mostly ortho-amphibole) is 0–15 vol.%. Because the ortho-amphibole (~265.9 $cm^3$/mol) has a molar volume about 4 times that of Opx (~62.7 $cm^3$/mol) at ambient conditions, the volume percentage of amphibole can be converted to a similar volume proportion of Opx (0–15 vol.%, denoted as Opx(1)) in an anhydrous mineral assemblage using the reaction coefficients in Eq. (5). This result is consistent with the fact that many dunite samples actually have a harzburgitic mineral modal composition (Fig. 6a), because a significant portion of Opx was consumed to form ortho-amphibole by retrograde metamorphism during the exhumation process. Based on the near-fractional melting model of a fertile lherzolite at low-pressure (1–3 GPa) and anhydrous conditions, 23–27% melting can consume about half of Opx and almost all Cpx, resulting in about 25 ± 5 vol.% Opx (denoted as Opx(2)) in a residual Ol–Opx–Cpx assemblage (Niu, 1997). Hence, it is estimated that about 5–30 vol.% Opx (Opx(2) – Opx(1)) must have been dissolved by the reactive percolating melt during the high-temperature boninitic melt–rock reaction. The measured Opx grains have a $Mg^{\#}$ of ~91–92, which can be imparted into the newly formed olivine ($olivine_4$), which has a consistent $Fo^{\#}$ (~91–93) that can be formed by successive Opx-consuming processes, namely partial melting, high-T melt–rock reaction and low-T fluid–rock reaction.

In contrast, tremolite has a wider P–T stability field than ortho-amphibole (Fig. 8). It appears at P–T conditions less than ~2 GPa and ~800 °C, at the expense of Opx and Cpx through the reaction:

$$5\underset{\text{Opx}}{(Mg,Fe)_2Si_2O_6} + 4\underset{\text{Cpx}}{Ca(Mg,Fe)Si_2O_6} + 2H_2O = \underset{\text{tremolite}}{2Ca_2(Mg,Fe)_5Si_8O_{22}(OH)_2} + 2\underset{\text{olivine}_4}{(Mg,Fe)_2SiO_4}\,. \quad (6)$$

The rare occurrence of tremolite in the matrix of dunite (Fig. 4b and d) is consistent with the nearly complete depletion of Cpx during partial melting and/or subsequent melt–rock reactions, whereas the presence of a dominant amphibole phase, tremolite, is in line with the high modal abundance of Cpx in olivine clinopyroxenite (Fig. 2f).

It is noteworthy that these low-T fluid–rock reactions or retrograde reactions as represented by the hydrous minerals in the matrix, mineral cleavages, and fractures, as well as monophase inclusions (representing healed cracks) in host minerals (Figs. 2, 3a, b, and 4a, d, e), are different from the formation of multiphase Mg- or Cr-rich hydrous silicate inclusions in the olivine and spinel (Figs. 3d and 4b–f). The latter is inferred to be crystallized from a volatile-rich boninitic melt (magmatic origin).

*6.6. Tectonic settings*

The tectonic setting that the Songshugou peridotites have experienced is a key issue for understanding the evolution history of the Qinling orogenic belt. The compositions of olivine and spinel are powerful petrogenetic indicators and can be used to discriminate the tectonic settings of peridotite (e.g., Arai, 1994; Dick and Bullen, 1984; Kamenetsky et al., 2001; Pearce et al., 2000).

Almost all harzburgite and spinel-poor coarse-grained, porphyroclastic, and fine-grained dunite fall within the region of modern forearc peridotites in the olivine $Fo^{\#}$ vs. NiO diagram (Fig. 5b; Ishii et al., 1992), whereas olivine grains from spinel-rich coarse-grained dunite show significantly higher $Fo^{\#}$ outside the region of forearc peridotites. Likewise, in the diagrams of spinel $Cr^{\#}$ vs. olivine $Fo^{\#}$ (Fig. 5a), spinel $Cr^{\#}$ vs. spinel $TiO_2$ (Fig. 5e) and spinel $Cr^{\#}$ vs. spinel $Mg^{\#}$ (Fig. 5f), almost all harzburgite and coarse-grained dunite show close relationships with peridotites associated with a high-Mg arc magma or boninite in a supra-subduction zone (SSZ) setting. This affinity to boninite is also shown in Fig. 5c and d, in which spinel grains in harzburgite and coarse-grained dunite plot in the boninite region. This boninitic signature can also be inferred from the observation of multiphase inclusions in olivine and spinel (Figs. 3d and 4b–f), which contain hydrous and carbonate phases that are rich in MgO and $Cr_2O_3$ and are thus consistent with a boninite origin.

**Fig. 7.** (a–e) Chondrite-normalized whole-rock REE patterns: (a) coarse-grained dunite, (b) fine-grained dunite, (c) coarse-grained harzburgite, (d) fine-grained harzburgite, and (e) olivine clinopyroxenite. Green solid lines are calculated chondrite-normalized REE patterns of residues after variable degrees (as labeled) of fractional melting of a depleted MOR mantle at spinel-facies condition (green dashed lines) (modified after Piccardo et al. (2007); and similar to Niu (2004) and Niu and Hekinian (1997)). (f–i) Chondrite-normalized whole-rock multi-element patterns: (f) coarse-grained dunite, (g) fine-grained dunite, (h) coarse-grained harzburgite, (i) fine-grained harzburgite, and (j) olivine clinopyroxenite. The multi-element patterns of dunite and harzburgite in the Torishima Forearc (red lines) and the Conical (green lines) Seamount at the Izu–Bonin–Mariana zone were also shown for comparison (Parkinson and Pearce, 1998). (For interpretation of the references to color in this figure legend, the reader is referred to the web version of this article.)

The genesis of boninite generally requires anomalously high mantle temperatures (i.e. T > 1100 °C) and a large fluid influx, so that an original refractory mantle can be further melted (Crawford, 1989; Fallon and Danyushevsky, 2000; Xia et al., 2012). These conditions are generally related to a young and warm forearc region (i.e. infant forearc) in a supra-subduction zone (Crawford, 1989; Kim and Jacobi, 2002). However, it is necessary to clarify that our argument does not suggest that partial melting occurs in the forearc mantle exclusively. Instead, partial melting has probably taken place in an episodic fashion (i.e. multistage melt depletion) in various tectonic environments. The latest melting event that is responsible for the generation of boninite (i.e. boninite-associated partial melting) only requires a small fraction of the originally refractory forearc mantle to continue to be melted (via melting Eq. (1)). The generation of this boninite is vital to explain the unique boninite-associated petrological and chemical signatures, as observed in the Songshugou harzburgite and dunite (see sections above), which can be attributed to the interaction between high-temperature boninitic melt and originally refractory mantle in an infant forearc setting. The highly refractory nature of the forearc mantle implies that the source of the forearc mantle must have already been intensively depleted during earlier melting events in other non-forearc settings (e.g., Dijkstra et al., 2010; Niu et al., 2003; Parkinson et al., 1998). In other words, the forearc peridotites should not be equated with melting residues purely formed in a forearc region. This argument has been corroborated by the ancient Os-isotope ages of modern forearc peridotites (e.g., Izu–Bonin–Mariana and Tonga) that carry potential implications concerning the initiation of a subduction zone as a consequence of a pre-existing lateral compositional buoyancy contrast within the oceanic lithosphere (Niu et al., 2003). This is expectedly the same case for the Songshugou dunite and harzburgite, though additional Os-isotope ages would certainly be helpful to confirm this idea.

As a potential evidence, Li et al. (2015) recently found boninite-like doleritic rocks in the early Paleozoic Shangdan suture zone where Songshugou ultramafic massif is situated. These boninite-like rocks display lower $TiO_2$ (0.09–0.41 wt.%) and FeO* [= FeO + 0.9 * $Fe_2O_3$] (4.3–10.25 wt.%) contents, lower Ti/V ratios and total REEs, and high Cr (303–1495 ppm) and Ni (102–383 ppm) values. In addition, they present two age periods: the older age of 524 Ma records the subduction initiation magmatism, whereas the younger age of 474 Ma is associated with backarc spreading.

Owing to the interactions with a high-T boninitic melt and a low-T $TiO_2$-rich aqueous fluid, dunite and harzburgite exhibit prominent enrichments of fluid-mobile LILEs (Fig. 7f–i), mimicking their counterparts in the Torishima Forearc and Conical Seamount in a modern (mature) forearc setting at the Izu–Bonin–Mariana subduction zone (Parkinson and Pearce, 1998; Spandler and Pirard, 2013). The low-T $TiO_2$-rich fluid–rock reaction in the temperature range of ~900–1100 °C likely indicates a forearc mantle that is being hydrated by slab-derived fluids at the incipient cooling stage of subduction zone. However, for those hydrous-silicate-forming low-T fluid–rock reactions, the scenarios could be different. The maximum P–T stability condition of Cr-chlorite ~900 °C at 3.5 GPa (Fischer et al., 2008) is consistent with a relatively cold thermal environment. This P–T condition could correspond to either forearc mantle in a mature subduction zone, or continental crust in a collisional belt, or both. In comparison, the maximum and negative-sloped P–T stabilities of both anthophyllite (from ~700 °C at ~0.5 GPa to ~650 °C at ~1 GPa) and tremolite (from ~820 °C at 0.5 GPa to ~650 °C at 2 GPa) imply that their formation is more likely related to a low-T fluid–rock reaction at a depth in orogenic crust in a continental collision belt.

Consequently, we postulated that the Songshugou harzburgite and dunite probably originally represent an ancient forearc lithospheric mantle which has undergone a boninite-associated partial melting and a subsequent high-T boninitic melt–rock reaction in a young and warm subduction zone. Afterwards, these peridotites experienced a series of low-T fluid–rock reactions that may occur either in a mature and cool subduction zone, or in an orogenic crust during their exhumation into the Qinling collisional orogeny at early Paleozoic era, or both.

### 6.7. Relationships between deformation and low-temperature fluid–rock reactions

Based on macro- and micro-structures of the Songshugou peridotites, decreasing strain can be manifested by the textural transition from fine-grained, through porphyroclastic, to coarse-grained dunite. The macroscopic lenticular and microscopic porphyroclastic textures (Figs. 1c and 2b) imply that coarse-grained dunite probably represents the remnant of ductile deformation and the precursor of its fine-grained counterpart, whereas porphyroclastic dunite could be regarded as the transition state. For those spinel-poor dunites, the spinel shows systematic increasing $X(Fe^{2+})$, $Y(Fe^{3+})$ and $Cr^{\#}$ from coarse- to fine-grained dunite, whereas the porphyroclastic dunite has bimodal compositions of spinel $X(Fe^{2+})$, $Y(Fe^{3+})$ and $Cr^{\#}$ similar to both coarse- and fine-grained dunites (Fig. 5a and c–f). The differences in spinel $Fe^{2+}$ content yield higher olivine–spinel equilibrium temperatures in coarse-grained (T = 826 ± 13 °C) compared to porphyroclastic (T = 799 ± 29 °C) and fine-grained (T = 757 ± 52 °C) dunite. Because (1) the diffusion of Mg and $Fe^{2+}$ between spinel and olivine is fairly fast and can continue to a temperature (~650 °C) that is lower than the estimated sub-solidus equilibrium temperatures of our peridotite samples (e.g., Henry and Medaris, 1980), and (2) spinel grains are more fractured in fine-grained and porphyroclastic dunites than coarse-grained dunite (Fig. 3), which results in smaller spinel grains and more effective diffusion of Mg and $Fe^{2+}$ in fine-grained and porphyroclastic dunites, the increase of spinel $Fe^{2+}$ content and decrease of the sub-solidus equilibrium temperature from coarse-grained, through porphyroclastic, to fine-grained dunite indicate that the re-equilibrium of mineral compositions between spinel and olivine was accelerated by ductile and/or brittle deformation. Similarly, the increasing spinel $Fe^{3+}$ content and $Cr^{\#}$ from coarse-grained, through porphyroclastic, to fine-grained dunite, implies that oxidation and low-T chlorite-forming fluid–rock reactions can also be enhanced by ductile and/or brittle deformation (cf. Fig. 3a and b–d).

In a similar manner, the higher spinel $TiO_2$ content in fine-grained dunite compared to porphyroclastic and coarse-grained dunites (Fig. 5e) can be attributed to the more intensive low-T $TiO_2$-rich fluid/rock reaction in fine-grained dunite, which is likely to be a consequence of the stronger ductile deformation it has experienced. The similar spinel $TiO_2$ content of porphyroclastic and coarse-grained dunites probably suggests that (1) $TiO_2$-rich fluid–rock reaction occurred at a higher temperature earlier than the low-temperature fluid–rock reaction forming chlorite and final re-equilibrium of the spinel composition with olivine; (2) the analyzed fine-grained dunite has been formed or was being developed by ductile deformation, while (3) the analyzed porphyroclastic dunite has not been differentiated from coarse-grained dunite when $TiO_2$-rich fluid–rock reaction was occurring; and thus (4) the studied porphyroclastic dunite was probably formed slightly earlier than and/or coeval with the chlorite-forming and final mineral re-equilibrium reactions, before brittle deformation started to be prevalent.

The olivine/orthopyroxene-crosscutting textures by amphibole crystals in a relatively random pattern, together with undeformed acicular monophase inclusions in olivine and orthopyroxene, clearly indicate that these amphibole-forming fluid–rock reactions mainly occurred at a brittle deformation regime. This inference of brittle condition is in agreement with the maximum P–T stability of the dominant amphibole phase anthophyllite (from ~700 °C at ~0.5 GPa to ~650 °C at ~1 GPa). This temperature is lower than that at which olivine can be significantly deformed plastically at a geological time scale, and the pressure corresponds to a depth in the crust shallower than the brittle–ductile transition for a olivine-rich rock (Kohlstedt et al., 1995).

The high-T boninitic melt–rock reaction is the key mechanism to form our spinel (chromite)-layered dunite. If we assume that the chromitite formation and associated melt–rock reaction occurred before the main ductile deformation event, we are expected to observe spinel (chromite)-rich samples in both coarse- and fine-grained dunite.

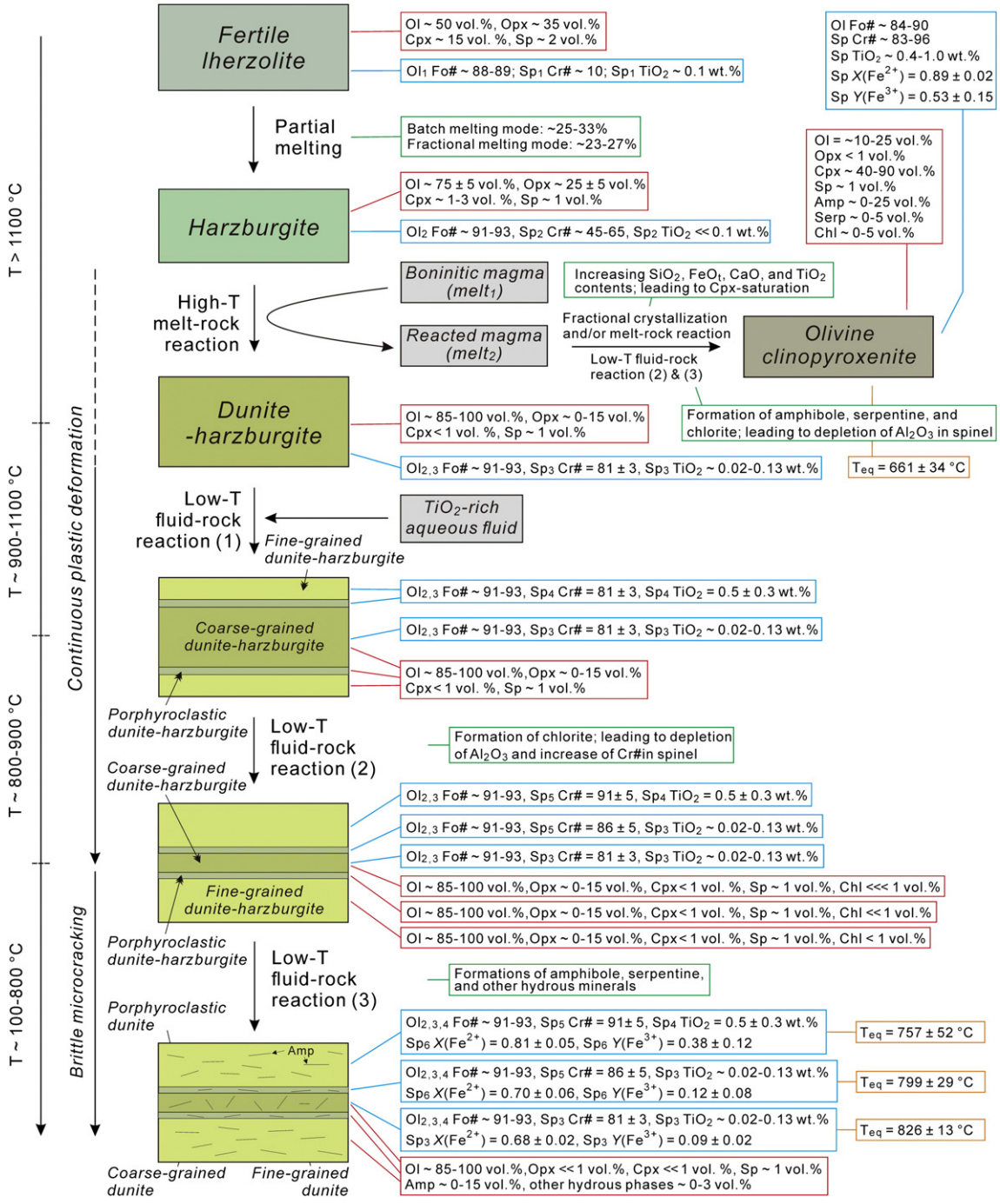


**Fig. 9.** Flow chart showing the major lithological and petrological evolutions of the Songshugou peridotites. The red and blue callouts describe the mineral volume proportions and compositions of olivine and spinel in each type of rock, respectively. The key characteristics of petrological processes and olivine–spinel equilibrium temperatures are also given in the green and yellow callouts, respectively. The subscripts of olivine and spinel correspond to those shown in the text. The distribution of fine-grained, porphyroclastic, and coarse-grained dunite–harzburgite schematically depicts the variations of their relative volume proportions with increasing plastic strain, which transforms the coarse-grained dunite–harzburgite into fine-grained dunite–harzburgite through their porphyroclastic intermediate. It should be noted that the distribution patterns of these texturally distinct dunite–harzburgite do not correspond to their actual spatial relationships in the field. (For interpretation of the references to color in this figure legend, the reader is referred to the web version of this article.)

However, the chromitite and spinel (chromite)-rich dunite seem to occur only in the coarse-grained dunite (see Fig. 1c). If this observation is true, then one possible explanation is that the chromitite and chromite-rich dunite might have not been preserved in the fine-grained dunite (i.e. altered by low-T fluid–rock reactions or retrograde metamorphisms), owing to the prolonged and intense ductile/brittle deformation in fine-grained dunite. Alternatively, the chromitite and chromite-rich dunite are also present within the fine-grained dunite, but they have not been discovered yet due to their small sizes and insufficient field mapping at present.

Nevertheless, we can still conclude that ductile and brittle deformations play an important role in affecting the petrological processes (Fig. 9). The prolonged and intense ductile/brittle deformation decreases the mineral grain size through plastic dynamic recrystallization and brittle fracturing, and thus increases the rock permeability by increasing the density of pathways for fluid diffusion and flow. This process eventually facilitates low-T fluid–rock reactions (metasomatism or retrograde metamorphism) and chemical re-equilibration between minerals in the fine-grained dunite.

## 7. Conclusion

In this study, the textures, mineral, and whole-rock chemical compositions of different types of peridotite were systemically analyzed. Based on these data, we can summarize the major lithological and petrological evolutions of the Songshugou peridotites as below (see Fig. 9 for details).

(1) The Songshugou ultramafic massif is dominated by fine- and coarse-grained dunite with minor harzburgite, olivine clinopyroxenite, and banded/podiform chromitite. The dunite and harzburgite probably represent highly refractory residues after episodic (i.e. multistage) high-degree melting events (25–33% batch melting or 23–27% fractional melting).
(2) The dunite and harzburgite had experienced an early-stage high-temperature melt–rock reaction as a result of a volatile-rich (i.e. $H_2O$ and $CO_2$) boninitic melt. Subsequently, these rocks suffered a late-stage low-temperature $TiO_2$-rich fluid–rock reaction.
(3) The remnant boninitic melt after boninitic melt–rock interaction was initially orthopyroxene-saturated and is thus able to form orthopyroxene-rich cumulate-like harzburgite during subsequent melt–rock reaction. Later, the remnant melt became progressively Cpx-saturated but still primitive in composition through a successive of fractional crystallization and/or melt–rock reactions, which was able to crystallize the dyke-like olivine clinopyroxenite.
(4) The young and warm forearc mantle (i.e. infant forearc) above a subducting slab is the site where both the boninite-generating associated partial melting and high-T melt–rock reactions are inferred to have occurred, whereas low-T fluid–rock reactions and coeval adjutant ductile/brittle deformation may occur either in a mature and cool subduction zone, or in an orogenic crust during their exhumation into the Qinling collisional orogeny at early Paleozoic era, or both.

Supplementary data to this article can be found online at http://dx.doi.org/10.1016/j.lithos.2016.03.002.

## Acknowledgments

We would like to thank Jinxue Du for his helpful discussions and tremendous assistance to draw phase equilibria diagrams. We also appreciate Guiming Shu and Xiaoli Li for conducting high-quality EPMA analyses at Peking University. Michael Roden and another anonymous reviewer as well as Editor Sun-Lin Chung were greatly appreciated for their thoughtful comments. This research is supported by the Major State Basic Research Development Projects (2015CB856105), National Natural Science Foundation of China (grant nos. 41572040, 41372060, 40825007, 41121062), and supported by Mid-career Researcher Program through NRF grant to H.J. funded by the MEST (no. 2015R1A2A1A15052305) and a BK21 + postdoctoral fellowship to Y.C. in Korea.

## References

Ague, J.J., Nicolescu, S., 2014. Carbon dioxide released from subduction zones by fluid-mediated reactions. Nature Geoscience 7, 355–360.
Arai, S., 1992. Chemistry of chromian spinel in volcanic-rocks as a potential guide to magma chemistry. Mineralogical Magazine 56, 173–184.
Arai, S., 1994. Characterization of spinel peridotites by olivine–spinel compositional relationships: review and interpretation. Chemical Geology 113, 191–204.
Arai, S., Yurimoto, H., 1994. Podiform chromitites of the Tari–Misaka ultramafic complex, southwestern Japan, as mantle–melt interaction products. Economic Geology 89, 1279–1288.
Arai, S., Matsukage, K., Isobe, E., Vysotskiy, S., 1997. Concentration of incompatible elements in oceanic mantle: effect of melt/wall interaction in stagnant or failed melt conduits within peridotite. Geochimica et Cosmochimica Acta 61, 671–675.
Arai, S., Abe, N., Ishimaru, S., 2007. Mantle peridotites from the Western Pacific. Gondwana Research 11, 180–199.
Ayers, J., Watson, E.B., 1993. Rutile solubility and mobility in supercritical aqueous fluids. Contributions to Mineralogy and Petrology 114, 321–330.
Bader, T., Zhang, L.F., Franz, L., Ratschbacher, L., de Capitani, C., 2012. The enigmatic Songshugou complex (Qinling orogen, central China): mélange of high-pressure and (ultra) high-temperature metamorphic rocks? 10th Swiss Geoscience Meeting, Bern, pp. 109–110
Ballhaus, C., Berry, R.F., Green, D.H., 1991. High pressure experimental calibration of the olivine–orthopyroxene–spinel oxygen geobarometer: implications for the oxidation state of the upper mantle. Contributions to Mineralogy and Petrology 107, 27–40.
Barnes, S.J., Roger, P.L., 2001. The range of spinel compositions in terrestrial mafic and ultramafic rocks. Journal of Petrology 42, 2279–2302.
Bédard, J.H., 2005. Partitioning coefficients between olivine and silicate melts. Lithos 83, 394–419.
Bédard, É., Hébert, R., Guilmette, C., Lesage, G., Wang, C.S., Dostal, J., 2009. Petrology and geochemistry of the Saga and Sangsang ophiolitic massifs, Yarlung Zangbo Suture Zone, Southern Tibet: evidence for an arc–back–arc origin. Lithos 113, 48–67.
Bodinier, J.L., Godard, M., 2007. 2.04 — Orogenic, Ophiolitic, and Abyssal Peridotites, in: Editors-in-Chief: Heinrich, D.H., Karl, K.T. (Eds.), Treatise on Geochemistry. Pergamon, Oxford, pp. 1–73.
Cao, Y., Jung, H., Song, S., Park, M., Jung, S., Lee, J., 2015. Plastic deformation and seismic properties in fore-arc mantles: a petrofabric analysis of the Yushigou harzburgites, North Qilian suture zone, NW China. Journal of Petrology 56, 1897–1944.
Chen, Z.H., 2004. The Neoproterozoic Tectono-thermal Events in the Qinling Orogen, and Their Geo-tectonic Significances. Chinese Academy of Geological Sciences, Beijing.
Chen, N.S., Han, Y.Q., You, Z.D., Sun, M., 1991. Whole-rock Sm–Nd, Rb–Sr, and single grain zircon Pb–Pb dating of complex rocks from the interior of the Qinling orogenic belt, Western Henan and its crustal evolution. Geochemica 20, 219–227.
Chen, D., Liu, L., Sun, Y., Zhang, A., Liu, X., Luo, J., 2004. LA-ICP-MS zircon U–Pb dating for high-pressure basic granulite from North Qinling and its geological significance. Chinese Science Bulletin 49, 2296–2304.
Crawford, A.J., 1989. Boninites. Unwin Hyman, London.
Dai, J.G., Wang, C.S., Hebert, R., Santosh, M., Li, Y.L., Xu, J.Y., 2011. Petrology and geochemistry of peridotites in the Zhongba ophiolite, Yarlung Zangbo Suture Zone: implications for the Early Cretaceous intra-oceanic subduction zone within the Neo-Tethys. Chemical Geology 288, 133–148.
Dare, S.A.S., Pearce, J.A., McDonald, I., Styles, M.T., 2009. Tectonic discrimination of peridotites using fO2–Cr# and Ga–Ti–FeIII systematics in chrome–spinel. Chemical Geology 261, 199–216.
Dick, H.J.B., 1989. Abyssal peridotites, very slow spreading ridges and ocean ridge magmatism. Journal of Geological Society, London, Special Publications 42, 71–105.
Dick, H.B., Bullen, T., 1984. Chromian spinel as a petrogenetic indicator in abyssal and alpine-type peridotites and spatially associated lavas. Contributions to Mineralogy and Petrology 86, 54–76.
Dick, H.J.B., Fisher, R.L., 1984. Mineralogic studies of the residues of mantle melting: abyssal and alpine-type peridotites. In: Kornprobst, J. (Ed.), Kimberlites II. The Mantle and Crust–Mantle Relationships. Elsevier, Amsterdam, pp. 298–308.
Dijkstra, A.H., Sergeev, D.S., Spandler, C., Pettke, T., Meisel, T., Cawood, P.A., 2010. Highly refractory peridotites on Macquarie Island and the case for anciently depleted domains in the Earth's mantle. Journal of Petrology 51, 469–493.
Dong, Y., Santosh, M., 2016. Tectonic architecture and multiple orogeny of the Qinling Orogenic Belt, Central China. Gondwana Research 29, 1–40.
Dong, Y.P., Zhou, M.F., Zhang, G.W., Zhou, D.W., Liu, L., Zhang, Q., 2008. The Grenvillian Songshugou ophiolite in the Qinling Mountains, Central China: implications for the tectonic evolution of the Qinling orogenic belt. Journal of Asian Earth Sciences 32, 325–335.
Edwards, S.J., Malpas, J., 1995. Multiple origins for mantle harzburgites: examples from the Lewis Hills, Bay of Islands ophiolite, Newfoundland. Canadian Journal of Earth Sciences 32, 1046–1057.
Evans, B.W., Frost, B.R., 1975. Chrome-spinel in progressive metamorphism—a preliminary analysis. Geochimica et Cosmochimica Acta 39, 959–972.
Fallon, T.J., Danyushevsky, L.V., 2000. Melting of refractory mantle at 1.5, 2 and 2.5 GPa under anhydrous and $H_2O$-undersaturated conditions: implications for the petrogenesis of high-Ca boninites and the influence of subduction components on mantle melting. Journal of Petrology 41, 257–283.
Fischer, J.K., Poli, S., Fumagalli, P., 2008. The effects of Cr solubility in chlorites and its implications for Cr-clinochlore stability. 12th International Conference on Experimental Mineralogy, Petrology and Geochemistry September 7th–10th 2008. Innsbruck University Press, Innsbruck, p. 23.
Gaetani, G.A., Grove, T.L., 1998. The influence of water on melting of mantle peridotite. Contributions to Mineralogy and Petrology 131, 323–346.
Goldstein, J., Newbury, D.E., Joy, D.C., Lyman, C.E., Echlin, P., Lifshin, P., Sawyer, L., Michael, J.R., 2003. Scanning Electron Microscopy and X-ray Microanalysis. Third edition. Springer, US.
Hellebrand, E., Snow, J.E., Dick, H.J.B., Hofmann, A.W., 2001. Coupled major and trace elements as indicators of the extent of melting in mid-ocean-ridge peridotites. Nature 410, 677–681.
Henry, D.J., Medaris, L.G., 1980. Application of pyroxene and olivine–spinel geothermometers to spinel peridotites in southwestern Oregon. American Journal of Science 280, 211–231.
Ionov, D.A., 2010. Petrology of mantle wedge lithosphere: new data on supra-subduction zone peridotite xenoliths from the andesitic Avacha Volcano, Kamchatka. Journal of Petrology 51, 327–361.
Irvine, T.N., 1965. Chromian spinel as a petrogenetic indicator: part 1. Theory. Canadian Journal of Earth Sciences 2, 648–672.

Ishii, T., Robinson, P.T., Maekawa, H., Fiske, R., 1992. 27. Petrological studies of peridotites from diapiric serpentinite seamounts in the Izu–Ogasawara–Mariana forearc, Leg 125. In: Fryer, P., Pearce, J.A., Stokking, L.B. (Eds.), Proceedings of the Ocean Drilling Program, Scientific Results, pp. 445–485.
Ishiwatari, A., 1985. Igneous petrogenesis of the Yakuno ophiolite (Japan) in the context of the diversity of ophiolites. Contributions to Mineralogy and Petrology 89, 155–167.
Jaques, A.L., Green, D.H., 1980. Anhydrous melting of peridotite at 0–15 Kb pressure and the genesis of tholeiitic basalts. Contributions to Mineralogy and Petrology 73, 287–310.
Kaczmarek, M.-A., Jonda, L., Davies, H., 2015. Evidence of melting, melt percolation and deformation in a supra-subduction zone (Marum ophiolite complex, Papua New Guinea). Contributions to Mineralogy and Petrology 170, 1–23.
Kamenetsky, V.S., Crawford, A.J., Meffre, S., 2001. Factors controlling chemistry of magmatic spinel: an empirical study of associated olivine, Cr-spinel and melt inclusions from primitive rocks. Journal of Petrology 42, 655–671.
Kelemen, P.B., Dick, H.J.B., Quick, J.E., 1992. Formation of harzburgite by pervasive melt/rock reaction in the upper mantle. Nature 358, 635–641.
Kelemen, P.B., Shimizu, N., Salters, V.J.M., 1995. Extraction of mid-ocean-ridge basalt from the upwelling mantle by focused flow of melt in dunite channels. Nature 375, 747–753.
Kim, J., Jacobi, R.D., 2002. Boninites: characteristics and tectonic constraints, northeastern Appalachians. Physics and Chemistry of the Earth 27, 109–147.
Kimball, K., 1990. Effects of hydrothermal alteration on the compositions of chromian spinels. Contributions to Mineralogy and Petrology 105, 337–346.
Kohlstedt, D.L., Evans, B., Mackwell, S.J., 1995. Strength of the lithosphere: constraints imposed by laboratory experiments. Journal of Geophysical Research 100, 17587–17602.
Lee, B., Zhu, L.M., Gong, H.J., Guo, B., Yang, T., Wang, F., Wang, W., Xu, A., 2010. Genetic relationship between peridotites and chromite deposit from Songshugou area of North Qinling. Acta Petrologica Sinica 26, 1487–1502.
Li, S.G., Chen, Y.Z., Zhang, G.W., Zhang, Z.Q., 1991. A 1 Ga B.P. Alpine peridotite body emplaced into the Qinling group: evidence for the existence of the late proterozoic plate tectonics in the north Qinling area. Geological Review 37, 235–242.
Li, C., Ripley, E., Sarkar, A., Shin, D., Maier, W., 2005. Origin of phlogopite–orthopyroxene inclusions in chromites from the Merensky Reef of the Bushveld Complex, South Africa. Contributions to Mineralogy and Petrology 150, 119–130.
Li, H.Y., Liu, J.F., Yang, L., 2009. Characteristics of zircons from a metamorphic contact zone of the Songshugou ultramafic pluton in North Qinling and their geological significance. Acta Petrologica Sinica 28, 225–234.
Li, Y., Yang, J.S., Dilek, Y., Zhang, J., Pei, X.Z., Chen, S.Y., Xu, X.Z., Li, J.Y., 2015. Crustal architecture of the Shangdan suture zone in the early Paleozoic Qinling orogenic belt, China: record of subduction initiation and backarc basin development. Gondwana Research 27, 733–744.
Liu, L., Zhou, D.W., Dong, Y.P., Zhang, H.F., Liu, Y.J., Zhang, Z.J., 1995. High pressure metabasites and their retrograde metamorphic P–T–t path from Songshugou area, Eastern Qinling Mountain. Acta Petrologica Sinica 11, 127–136.
Liu, J.F., Sun, W.D., Sun, Y., Sun, Y.L., Liu, F.J., 2007. Geochemistry and platinum-group elements of ultramafic rocks from the Songshugou area in the Eastern Qinling: constraints on petrogenesis. Geological Review 53, 1–8.
Liu, J.F., Sun, Y., Tong, L.X., Sun, W.D., 2009. Emplacement age of the Songshugou ultramafic massif in the Qinling orogenic belt, and geologic implications. International Geology Review 51, 58–76.
Lorand, J.P., Cottin, J.Y., 1987. Na–Ti–Zr–$H_2O$-rich mineral inclusions indicating postcumulus chrome-spinel dissolution and recrystallization in the Western Laouni mafic intrusion, Algeria. Contributions to Mineralogy and Petrology 97, 251–263.
Matsukage, K., Arai, S., 1998. Jadeite, albite and nepheline as inclusions in spinel of chromitite from Hess Deep, equatorial Pacific: their genesis and implications for serpentinite diapir formation. Contributions to Mineralogy and Petrology 131, 111–122.
Matsukage, K.N., Kubo, K., 2003. Chromian spinel during melting experiments of dry peridotite (KLB-1) at 1.0–2.5 GPa. American Mineralogist 88, 1271–1278.
Melcher, F., Grum, W., Simon, G., Thalhammer, T.V., Stumpfl, E.F., 1997. Petrogenesis of the ophiolitic giant chromite deposits of Kempirsai, Kazakhstan: a study of solid and fluid inclusions in chromite. Journal of Petrology 38, 1419–1458.
Meng, Q.R., Zhang, G.W., 2000. Geologic framework and tectonic evolution of the Qinling orogen, central China. Tectonophysics 323, 183–196.
Merle, R., Kaczmarek, M.-A., Tronche, E., Girardeau, J., 2012. Occurrence of inherited supra-subduction zone mantle in the oceanic lithosphere as inferred from mantle xenoliths from Dragon Seamount (southern Tore–Madeira Rise). Journal of the Geological Society 169, 251–267.
Merlini, A., Grieco, G., Diella, V., 2009. Ferritchromite and Cr-chlorite formation in Kalkan serpentinitic melange (Southern Urals, Russia). American Mineralogist 94, 1459–1467.
Niu, Y., 1997. Mantle melting and melt extraction processes beneath ocean ridges: evidence from abyssal peridotites. Journal of Petrology 38, 1047–1074.
Niu, Y., 2004. Bulk-rock major and trace element compositions of abyssal peridotites: implications for mantle melting, melt extraction and post-melting processes beneath mid-ocean ridges. Journal of Petrology 45, 2423–2458.
Niu, Y., 2005. Generation and evolution of basaltic magmas: some basic concepts and a hypothesis for the origin of the Mesozoic–Cenozoic volcanism in eastern China. Geological Journal of China Universities 11, 9–46.
Niu, Y., Hekinian, R., 1997. Basaltic liquids and harzburgitic residues in the Garrett Transform: a case study at fast-spreading ridges. Earth and Planetary Science Letters 146, 243–258.
Niu, Y., Langmuir, C.H., Kinzler, R.J., 1997. The origin of abyssal peridotites: a new perspective. Earth and Planetary Science Letters 152, 251–265.
Niu, Y., O'hara, M.J., Pearce, J.A., 2003. Initiation of subduction zones as a consequence of lateral compositional buoyancy contrast within the lithosphere: a petrological perspective. Journal of Petrology 44, 851–866.
Obata, M., Banno, S., Mori, T., 1974. The iron–magnesium partitioning between naturally occurring coexisting olivine and Ca-rich clinopyroxene: an application of the simple mixture model to olivine solid solution. Bulletin de la Societe Francaise de Mineralogie et de Cristallographie 97, 101–107.
Okay, A.I., Şengör, A.M.C., Satir, M., 1993. Tectonics of an ultrahigh-pressure metamorphic terrane: the Dabie Shan/Tongbai Shan Orogen, China. Tectonics 12, 1320–1334.
Pal, T., 2011. Petrology and geochemistry of the Andaman ophiolite: melt–rock interaction in a suprasubduction-zone setting. Journal of the Geological Society 168, 1031–1045.
Parkinson, I.J., Pearce, J.A., 1998. Peridotites from the Izu–Bonin–Mariana Forearc (ODP Leg 125): evidence for mantle melting and melt–mantle interaction in a supra-subduction zone setting. Journal of Petrology 39, 1577–1618.
Parkinson, I.J., Pearce, J.A., Thirlwall, M.F., Johnson, K.T.M., Ingram, G., 1992. 28. Trace element geochemistry of peridotites from the Izu–Bonin–Mariana forearc, Leg 125. Proceeding of the Ocean Drilling Program, Scientific Results 125, 487–506.
Parkinson, I.J., Hawkesworth, C.J., Cohen, A.S., 1998. Ancient mantle in a modern arc: osmium isotopes in Izu–Bonin–Mariana forearc peridotites. Science 281, 2011–2013.
Pearce, J.A., van der Laan, S.R., Arculus, R.J., Murton, B.J., Ishii, T., Peate, D.W., Parkinson, I.J., 1992. 38. Boninite and harzburgite from Leg 125 (Bonin–Mariana Forearc): a case study of magma genesis during the initial stages of subduction. Proceeding of the Ocean Drilling Program, Scientific Results 125, 623–659.
Pearce, J.A., Barker, P.F., Edwards, S.J., Parkinson, I.J., Leat, P.T., 2000. Geochemistry and tectonic significance of peridotites from the South Sandwich arc–basin system, South Atlantic. Contributions to Mineralogy and Petrology 139, 36–53.
Piccardo, G.B., Zanetti, A., Muntener, O., 2007. Melt/peridotite interaction in the Southern Lanzo peridotite: field, textural and geochemical evidence. Lithos 94, 181–209.
Poli, S., 2015. Carbon mobilized at shallow depths in subduction zones by carbonatitic liquids. Nature Geoscience (advance online publication).
Powell, R., Holland, T., Worley, B., 1998. Calculating phase diagrams involving solid solutions via non-linear equations, with examples using THERMOCALC. Journal of Metamorphic Geology 16, 577–588.
Rapp, J.F., Klemme, S., Butler, I.B., Harley, S.L., 2010. Extremely high solubility of rutile in chloride and fluoride-bearing metamorphic fluids: an experimental investigation. Geology 38, 323–326.
Ratschbacher, L., Hacker, B.R., Calvert, A., Webb, L.E., Grimmer, J.C., McWilliams, M.O., Ireland, T., Dong, S.W., Hu, J.M., 2003. Tectonics of the Qinling (Central China): tectonostratigraphy, geochronology, and deformation history. Tectonophysics 366, 1–53.
Renna, M.R., Tribuzio, R., 2011. Olivine-rich troctolites from Ligurian Ophiolites (Italy): evidence for impregnation of replacive mantle conduits by MORB-type melts. Journal of Petrology 52, 1763–1790.
Saka, S., Uysal, I., Akmaz, R.M., Kaliwoda, M., Hochleitner, R., 2014. The effects of partial melting, melt–mantle interaction and fractionation on ophiolite generation: constraints from the late Cretaceous Pozantı–Karsantı ophiolite, southern Turkey. Lithos 202–203, 300–316.
Schiano, P., Clocchiatti, R., Lorand, J.-P., Massare, D., Deloule, E., Chaussidon, M., 1997. Primitive basaltic melts included in podiform chromites from the Oman Ophiolite. Earth and Planetary Science Letters 146, 489–497.
Song, S.G., Su, L., Yang, H.Q., Wang, Y.S., 1998. Petrogenesis and emplacement of the Songshugou peridotite in Shangnan, Shaanxi. Acta Petrologica Sinica 14, 212–221.
Song, S.G., Zhang, L.F., Niu, Y.L., 2004. Ultra-deep origin of garnet peridotite from the North Qaidam ultrahigh-pressure belt, Northern Tibetan Plateau, NW China. American Mineralogist 89, 1330–1336.
Song, S.G., Su, L., Niu, Y.L., Lai, Y., Zhang, L.F., 2009. CH4 inclusions in orogenic harzburgite: evidence for reduced slab fluids and implication for redox melting in mantle wedge. Geochimica et Cosmochimica Acta 73, 1737–1754.
Song, S.G., Niu, Y.L., Su, L., Xia, X.H., 2013. Tectonics of the North Qilian orogen, NW China. Gondwana Research 23, 1378–1401.
Soustelle, V., Tommasi, A., Demouchy, S., Ionov, D.A., 2010. Deformation and fluid–rock interaction in the supra-subduction mantle: microstructures and water contents in peridotite xenoliths from the Avacha volcano, Kamchatka. Journal of Petrology 51, 363–394.
Spandler, C., Pirard, C., 2013. Element recycling from subducting slabs to arc crust: a review. Lithos 170, 208–223.
Spandler, C.J., Eggins, S.M., Arculus, R.J., Mavrogenes, J.A., 2000. Using melt inclusions to determine parent-magma compositions of layered intrusions: application to the Greenhills Complex (New Zealand), a platinum group minerals-bearing, island–arc intrusion. Geology 28, 991.
Spandler, C., Mavrogenes, J., Arculus, R., 2005. Origin of chromitites in layered intrusions: evidence from chromite-hosted melt inclusions from the Stillwater Complex. Geology 33, 893–896.
Su, L., Song, S.G., Song, B., Zhou, D.W., Hao, J.R., 2004. SHRIMP zircon U–Pb ages of garnet pyroxenite and Fushui gabbroic complex in Songshugou region and constraints on tectonic evolution of Qinling orogenic belt. Chinese Science Bulletin 49, 1146–1157.
Su, L., Song, S.G., Zhou, D.W., 2005. Petrogenesis of Songshugou dunite body in the Qinling orogenic belt, Central China: constraints from geochemistry and melt inclusions. Science in China Series D-Earth Sciences 48, 1146–1157.
Sun, W., Williams, I.S., Li, S., 2002. Carboniferous and Triassic eclogites in the western Dabie Mountains, east-central China: evidence for protracted convergence of the North and South China Blocks. Journal of Metamorphic Geology 20, 873–886.
Takahashi, E., Uto, K., Schiling, J.G., 1987. Primary magma compositions and Mg/Fe ratios of their mantle residues along Mid Atlantic Ridge 29°N to 73°N. Technical Reports ISEI, pp. 1–4.
Tang, L., Santosh, M., Dong, Y., Tsunogae, T., Zhang, S., Cao, H., 2016. Early Paleozoic tectonic evolution of the North Qinling orogenic belt: evidence from geochemistry, phase equilibrium modeling and geochronology of metamorphosed mafic rocks from the Songshugou ophiolite. Gondwana Research 30, 48–64.

Tian, W., Chen, B., Ireland, T.R., Green, D.H., Suzuki, K., Chu, Z., 2011. Petrology and geochemistry of dunites, chromitites and mineral inclusions from the Gaositai Alaskan-type complex, North China Craton: implications for mantle source characteristics. Lithos 127, 165–175.

Umino, S., Kitamura, K., Kanayama, K., Tamura, A., Sakamoto, N., Ishizuka, O., Arai, S., 2015. Thermal and chemical evolution of the subarc mantle revealed by spinel-hosted melt inclusions in boninite from the Ogasawara (Bonin) Archipelago, Japan. Geology 43, 151–154.

Uysal, I., Akmaz, R.M., Kapsiotis, A., Demir, Y., Saka, S., Avcı, E., Müller, D., 2015. Genesis and geodynamic significance of chromitites from the Orhaneli and Harmancık ophiolites (Bursa, NW Turkey) as evidenced by mineralogical and compositional data. Ore Geology Reviews 65, 26–41.

van der Laan, S.R., Arculus, R.J., Pearce, J.A., Murton, B.J., 1992. 10. Petrography, mineral chemistry, and phase relations of the basement boninite series of site 786, Izu–Bonin forearc. Proceeding of the Ocean Drilling Program, Scientific Results 125, 171–201.

Veksler, I.V., Nielsen, T.F.D., Sokolov, S.V., 1998. Mineralogy of crystallized melt inclusions from Gardiner and Kovdor ultramafic alkaline complexes: implications for carbonatite genesis. Journal of Petrology 39, 2015–2031.

Wang, T., Wang, X., Zhang, G., Pei, X., Zhang, C., 2003. Remnants of a Neoproterozoic collisional orogenic belt in the core of the Phanerozoic Qinling orogenic belt (China). Gondwana Research 6, 699–710.

Wang, X.B., Yang, J.S., Shi, R.D., Chen, S.Y., 2005. The Songshugou rock body from Qinling — a example of ultramafic cumulate undergone amphibole facies metamorphism. Acta Geologica Sinica 79, 174–189.

Warren, J.M., 2016. global variations in abyssal peridotite compositions. Lithos.

Xia, X., Song, S., Niu, Y., 2012. Tholeiite–boninite terrane in the North Qilian suture zone: implications for subduction initiation and back–arc basin development. Chemical Geology 328, 259–277.

Yang, J.J., Powell, R., 2008. Ultrahigh-pressure garnet peridotites from the devolatilization of sea-floor hydrated ultramafic rocks. Journal of Metamorphic Geology 26, 695–716.

Yang, J., Xu, Z., Dobrzhinetskaya, L.F., Green, H.W., Pei, X., Shi, R., Wu, C., Wooden, J.L., Zhang, J., Wan, Y., Li, H., 2003. Discovery of metamorphic diamonds in central China: an indication of a >4000-km-long zone of deep subduction resulting from multiple continental collisions. Terra Nova 15, 370–379.

Yu, H., Zhang, H.-F., Li, X.-H., Zhang, J., Santosh, M., Yang, Y.-H., Zhou, D.-W., 2016. Tectonic evolution of the North Qinling Orogen from subduction to collision and exhumation: evidence from zircons in metamorphic rocks of the Qinling Group. Gondwana Research 30, 65–78.

Zhang, Z.J., 1995. The genesis of dunites in the Songshugou ultramafic rock body, North Qinling. Acta Petrologica Sinica 11, 178–189.

Zhou, M.F., Robinson, P.T., Bai, W.J., 1994. Formation of podiform chromitites by melt/rock interaction in the upper mantle. Mineralium Deposita 29, 98–101.

Zhou, M.F., Robinson, P.T., Malpas, J., Li, Z.J., 1996. Podiform chromitites in the Luobusa ophiolite (Southern Tibet): implications for melt-rock interaction and chromite segregation in the upper mantle. Journal of Petrology 37, 3–21.

Zhou, M.F., Robinson, P.T., Malpas, J., Edwards, S.J., Qi, L., 2005. REE and PGE geochemical constraints on the formation of dunites in the Luobusa ophiolite, southern Tibet. Journal of Petrology 46, 615–639.